Research in Veterinary Science 209 (2026) 106249

Contents lists available at ScienceDirect

Research in Veterinary Science

journal homepage: www.elsevier.com/locate/rvsc

Acute effects of Cold Atmospheric Plasma on bottlenose dolphin skin fibroblasts: Implications for wound healing in cetaceans

Alice Gonella [a], Leonardo Zampieri [b], Livio Finos [c], Matteo Zuin [d], Anna Perazzi [e,**], Giuseppina Covello [f], Marta Giacomello [f], Cinzia Centelleghe [a], Emilio Martines [b], Antonella Peruffo [a,*]

[a] Department of Comparative Biomedicine and Food Science, University of Padova, Padova, Italy
[b] Department of Physics "Giuseppe Occhialini", University of Milano-Bicocca, Milano, Italy
[c] Department of Statistical Sciences, University of Padova, Padova, Italy
[d] Consorzio RFX (CNR, ENEA, INFN, University of Padova, Acciaierie Venete SpA), Padova, Italy
[e] Department of Animal Medicine, Production and Health, University of Padua, Padova, Italy
[f] Department of Biology, University of Padua, Padua, Italy

ARTICLE INFO

Keywords:
Cold Atmospheric Plasma (CAP)
Fibroblasts
Tursiops truncatus
Cell viability
Cell cycle

ABSTRACT

Skin lesions are common in cetaceans and are challenging to treat due to environmental exposure and difficulties in administering therapies. Cold Atmospheric Plasma (CAP) is a non-invasive approach that may promote wound healing and reduce microbial infections through the generation of reactive oxygen and nitrogen species. Dermal fibroblasts play a central role in tissue repair, particularly in extracellular matrix production and wound contraction, making them key targets to evaluate CAP's therapeutic potential.

In this study, a dermal fibroblasts cell line from bottlenose dolphins was exposed to short exposure (1, 2, 5 min) and long exposure (10 min) and analyzed at 0, 4, and 8 h post-treatment. Cell viability and cell cycle dynamics were assessed using MTT assays and high-content imaging. High-content imaging was employed to quantitatively evaluate cell cycle distribution and nuclear morphology through automated image analysis. Short CAP exposure enhanced cell cycle progression, increasing the proportion of cells in S and G2/M phases, whereas prolonged exposure induced early cell cycle alterations and led to nuclear collapse.

These results indicate that CAP effects on fibroblasts are time-dependent with short exposures promoting early pro-survival and cell cycle–related responses, and longer exposures inducing cytotoxicity. Further studies are required to determine whether these early responses translate into sustained proliferative or regenerative effects and to optimize CAP protocols for potential therapeutic applications in cetacean skin repair.

1. Introduction

In recent years, CAPs have arisen as a promising technology in biological and medical treatments (Morabit et al., 2021).

CAP is a promising therapeutic approach also for treating skin wounds in animals. In sheep wound models, it was demonstrated that plasma treatment induced an increase in keratinocytes proliferation of the basal layer of the epidermis, which improved the formation of cutaneous adnexa, and also reduced inflammation and promoted angiogenesis (Martines et al., 2020). Reactive Oxygen and Nitrogen Species (RONS) fundamentally influence the physiology of living cells; for example by inducing oxidative stress; which can alter cell proliferation; trigger apoptosis; and modulate signaling pathways; ultimately affecting tissue function and organismal health (Brun et al., 2014).

While excessive RONS levels can lead to apoptosis in eukaryotic cells or cause bactericidal and virucidal effects (Nicol et al., 2020; Redza-Dutordoir and Averill-Bates, 2016), moderate and controlled RONS concentrations can positively influence cell signaling pathways,

* Correspondence to: Antonella Peruffo, Department of Comparative Biomedicine and Food Science, University of Padova, viale dell'Università 16, 35020 Legnaro, PD, Italy.
** Correspondence to: Anna Perazzi, Department of Animal Medicine, Production and Health, Biomedicine and Food Science, University of Padova, viale dell'Università 16, 35020 Legnaro, PD, Italy.
E-mail addresses: Anna.perazzi@unipd.it (A. Perazzi), antonella.peruffo@unipd.it (A. Peruffo).

https://doi.org/10.1016/j.rvsc.2026.106249
Received 12 June 2025; Received in revised form 18 April 2026; Accepted 5 May 2026
Available online 18 May 2026

stimulating processes such as proliferation, migration, and angiogenesis key events in wound healing (Busco et al., 2020; Arndt et al., 2013).

Skin lesions and ulcerative dermatitis caused by environmental factors, bacteria, viruses, fungi, and protozoa, are a common and persistent problem in cetaceans, often localized around body orifices and sometimes becoming extensive, granular, or ulcerated (Van Bressem et al., 2024; Segura-Göthlin et al., 2023; Duignan et al., 2020; Toms et al., 2021; Van Bressem et al., 1999).

Current therapeutic options for these lesions remain limited, with treatment often relying on a combination of surgical excision and highest recommended doses of antibiotics, an approach that frequently results in incomplete healing or recurrence, highlighting the urgent need for new therapeutic strategies (Kamio et al., 2025). Moreover; controlling disease progression is further complicated by the emergence of resistance to multiple antibiotics agents (Inano et al., 2013).

CAP may facilitate wound healing in cetaceans through a dual mechanism: first, via its direct antimicrobial action, where reactive oxygen generated by CAP reduce microbial load by damaging microbial membranes, proteins, and DNA (Zhang et al., 2023); thereby promoting wound decontamination and lowering infection risk. Second; through a modulatory effect on skin cells; particularly fibroblasts by stimulating their proliferation; extracellular matrix production; and tissue regeneration; all of which are critical for wound closure and repair (Roux et al., 2025).

Our objective was to evaluate the effects of CAP treatment on fibroblasts derived from the skin of bottlenose dolphins and to provide insights into its mechanisms of action. Despite keratinocytes are central to epidermal regeneration through re-epithelialization, fibroblasts play an equally critical role in wound healing particularly during the proliferative and remodeling phases by promoting cell proliferation and extracellular matrix deposition. These processes have been shown to be enhanced by CAP (Brun et al., 2014; Martines et al., 2020). As cetacean skin lesions often involve full-thickness dermal damage, characterizing fibroblast responses is essential to enhance our understanding of CAP's therapeutic potential in marine mammal wound repair.

While many studies highlight the diverse biomedical applications of CAP, the CAP-based therapeutic approach still faces significant limitations, such as the poor control of generated RONS and limited understanding of its cellular mechanisms (Chupradit et al., 2023). As such; optimization of its therapeutic potential requires the development of standardized protocols to identify the most effective plasma treatment schemes (Tornin et al., 2021).

In this study, we investigated the effects of CAP treatment on fibroblasts derived from bottlenose dolphin skin by examining a range of treatment durations (1, 2, 5 and 10 min). We evaluated cell viability and changes in cell-cycle progression at the incubation periods (0, 4, and 8 h) following CAP treatment. These timepoints were designed to bracket the therapeutic window while considering the unique characteristics of cetacean dermal tissue, which in vivo may require deeper penetration than what is typically observed in standard single-cell in vitro assays. The selected exposure times are also in analogy to a previous study on fibroblast-like primary cells made by some members of our research group with a low-power helium plasma (Brun et al., 2014). Given the critical role of fibroblasts in wound healing, particularly during the proliferative and remodeling phases, understanding their response to CAP is crucial for developing effective new treatment strategies for cetacean skin lesions, which currently lack satisfactory therapeutic options.

In this context, CAP could represent a promising new therapy for skin lesions in cetacean. Its antimicrobial and proliferative properties could help to treat lesions by stimulating healing and reducing infection.

The present work is an attempt to find new effective therapeutic strategies to treat skin lesions in cetaceans.

2. Materials and methods

2.1. Cell line establishment and maintaining

The *Tursiops truncatus* fibroblast cell line was established and characterized following a laboratory protocol (Otero-Sabio et al., 2022). The cell line is maintained in a medium consisting of a 1:1 mixture of DMEM and Ham's F-12 (Biowest®, Nuaillé, France), supplemented with penicillin (30 mg/l), streptomycin (50 mg/l) (Pan Biotech™, Aidenbach, Germany) and 10% fetal bovine serum (FBS Good, Pan Biotech™, Aidenbach, Germany). Skin fibroblasts can be cryopreserved at −80 °C in a cryopreservation medium consisting of a mixture of 90% (*v*/v) FBS and 10% (v/v) dimethyl sulfoxide (DMSO). This cell line belongs to the patent Sea Sentinels System (S.S.S.) (patent n°102,020,000,003,248; https://www.knowledge-share.eu/en/patent/sea-sentinel-system-for-environmental-studies/).

2.2. Plasma source

A custom CAP source has been designed and realized for this experiment; an array of 8 plasma jets, properly spaced, has been realized such that a whole column of a 96-wells plate can be treated at once. Each jet consists in a cropped Pasteur pipette, in which a copper electrode is axially fixed; an aluminum bar placed at the level of the pipette tips acts as second grounded electrode (Fig. 1).

Helium is flown at a rate of 4 l/min, corresponding to 0.5 l/min in each pipette. When, using a resonant power supply, a sinusoidal voltage (5.2 kV peak-to-peak, 5.0 kHz) is applied to the central rod, cold plasma develops inside the pipette and travels outside from the nozzle, resulting in a plasma plume on the mixing layer between helium flow and atmospheric air; the glass of each pipette acts as a dielectric between the central rod and the external ground, preventing the transition of the discharge to an arc. A set of 21.7 kΩ ballast resistors, placed between each electrode and the power supply, allows to keep the electrodes balanced and to avoid current spikes. A preliminary study concerning the thermal load to the treated surface has been conducted, performing similar treatments on mock solutions and measuring with a thermocouple the temperature of the samples before and after the plasma exposure: a temperature increases lower than 1 degree was found, thus ruling out thermal effects.

The system is fixed in position by a custom-built structure, which allows the source to be in a stable and reproducible position with respect to the treated samples. In particular, the nozzle is fixed 8 mm above the culture media surface. The plasma plume is around 1 cm long when allowed to develop without hitting a target, with a stable appearance.

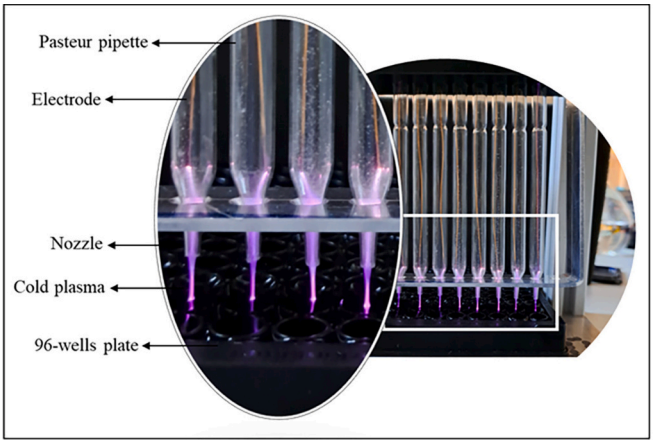

Fig. 1. Image of the plasma source used for treatments, displaying the eight helium plasma jets in operation. Each jet is directed into the wells of the plate where the cells are seeded.

When the plasma is generated, plasma plume comes into contact with the culture medium surface. The time behavior of the high voltage applied to the electrodes has been measured with a Rhode&Schwarz RTH1004 battery-powered oscilloscope and a Tektronix P6015a high voltage probe. The current flowing into the plasma, detected as voltage drop over a 10 Ω shunt resistor which has been added to the circuit, has also been measured. Typical waveforms of these two quantities are shown in Fig. 2A. It can be seen that the voltage is sinusoidal, with an amplitude of 1.8 kV and a frequency of 5 kHz. The current consists of a capacitive oscillation with superimposed spikes, which develop in the proximity of the voltage peaks. These spikes correspond to the streamers, also called plasma bullets in the literature, which develop in this kind of plasma jet, and which are associated with the power transfer to the plasma. From the product of the two quantities, the instantaneous power shown in Fig. 2B, is obtained. It shows an oscillation with a period double that of the voltage (as could be expected), which has zero average and does not contribute to the mean power. Superimposed to this are peaks associated to the streamers, reaching instantaneous values up to 30 W. Averaging over a voltage period, the average power transferred to the plasma has been shown to be 1.11 ± 0.05 W. This confirms that this plasma source is quite mild, if compared to others present in the literature. This average power value was found to be reproducible over multiple measurements. It has been checked that these measurements have the same values over all the eight jets, confirming the hypothesis of their equivalence in terms of chemical and biological effects.

2.3. MTT cell viability and toxicity assay

Tursiops truncatus fibroblasts were plated at a density of 1 × 10^4 cells/well in 96-well plates (Sarstedt), and maintained in the incubator under standard conditions at 37 °C with 5% CO2 and humidified atmosphere. After 24 h, cells were exposed to CAP treatment for different exposure times: 1, 2, 5, and 10 min. As positive control, cells were exposed to Thapsigargin at different concentration: 4 μM, 0.4 μM, 0.04 μM, 0.004 μM and 0.0004 μM. Thapsigargin was used as a positive control across a range of concentrations, consistent with previous in vitro studies demonstrating dose-dependent cellular responses used to characterize effects on fibroblast-like cells (Wang et al., 2014) and on adipocytes in vitro (Kamiya et al., 2013). Thapsigargin incubation was performed for 30 min in parallel to CAP-treated cells. For incubation period of 0 h; 4 h and 8 h; cells were incubated with Thapsigargin for 30 min in parallel to CAP-treated cells and subsequently replaced with fresh medium until the end of the incubation period. Non-treated cells were used as negative control. After CAP treatment cells were incubated at 37 °C and 5% CO_2 for three different incubation periods: 0; 4 and 8 h. Cell viability was evaluated using the MTT [3-(4;5-dimethylthiazol-2-yl)-2;5-diphenyltetrazolium bromide] assay. In detail; 10 μL MTT (5 mg/ml dye) solution (Thermo Fisher Scientific; Waltham; MA; USA) were added per well; and cells were incubated for 2 h at 37 °C. MTT is a yellow; water-soluble tetrazolium salt. Living cells have active mitochondria that reduce MTT to formazan; an insoluble purple crystal. The amount of formazan produced is directly proportional to the number of viable (metabolically active) cells and this reaction is only evidenced in viable mitochondria (Solan et al., 2022). The reaction was stopped by adding 20 μl/well of solubilization solution (composed by SDS: 20%; 50% DMF; acetic acid 2%; adjusted to a final volume of 200 mL with distilled water). Plates were covered in the dark and placed on a shaker at 90 rpm overnight at room temperature to ensure complete solubilization of the formazan crystals. Finally; absorbance for each well was measured using the multilabel plate reader VICTOR™ X4 (PerkinElmer®; Waltham; MA; USA) at 590 nm. To assess cell viability; the ratio of the absorbance of treated cells/absorbance of control cells; expressed in percentage; was calculated (Mosmann, 1983). For each incubation period (0 h, 4 h, and 8 h), three independent experiments were performed on separately seeded plates. In each experiment, 16 replicates per condition (1, 2, 5, and 10 min) were included. Non-treated cells were used as control.

2.4. Experimental design of cold plasma treatment

Cells were seeded at a density of 1 × 10^4 cells/well in a 96-well ViewPlate-96 F TC (Revvity®, Waltham, MA, USA). For each well, 250 μl/well of culture medium was used. After 24 h, cells were exposed to CAP treatment for different exposure times: 1, 2, 5, and 10 min.

After CAP treatment, cells were incubated at 37 °C and 5% CO2, considering three incubation periods: 0, 4 and 8 h. The culture medium was not replaced after CAP treatment. The fixation with 4% paraformaldehyde (PFA) was performed for 15 min at room temperature.

After fixation, the cells were washed three times with phosphate-buffered saline (PBS) (Gibco, Life Technologies, Monza, Italy) and were counter-stained with Hoechst 33342 (Gibco, Life Technologies, Monza, Italy), diluted 1:10,000 in PBS for 30 min at room temperature (Fig. 3). After the incubation period, the cells were washed three times with PBS. Following the washes, 100 μl of PBS was added to each well, and the samples were analyzed using High-Throughput Screening (HTS) analysis (Fig. 3). Three independent experiments were performed for each incubation period, each with eight replicates per condition.

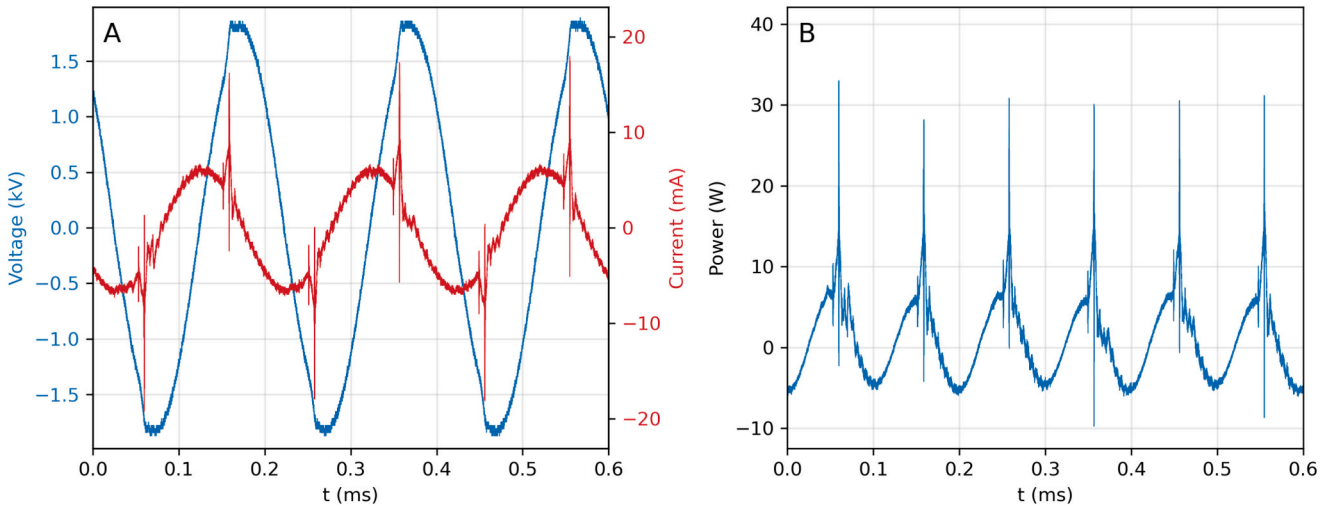

Fig. 2. Left: waveforms of the voltage and current measured on one of the eight electrodes. Right: waveform of the power, obtained as the product of the voltage by the current.

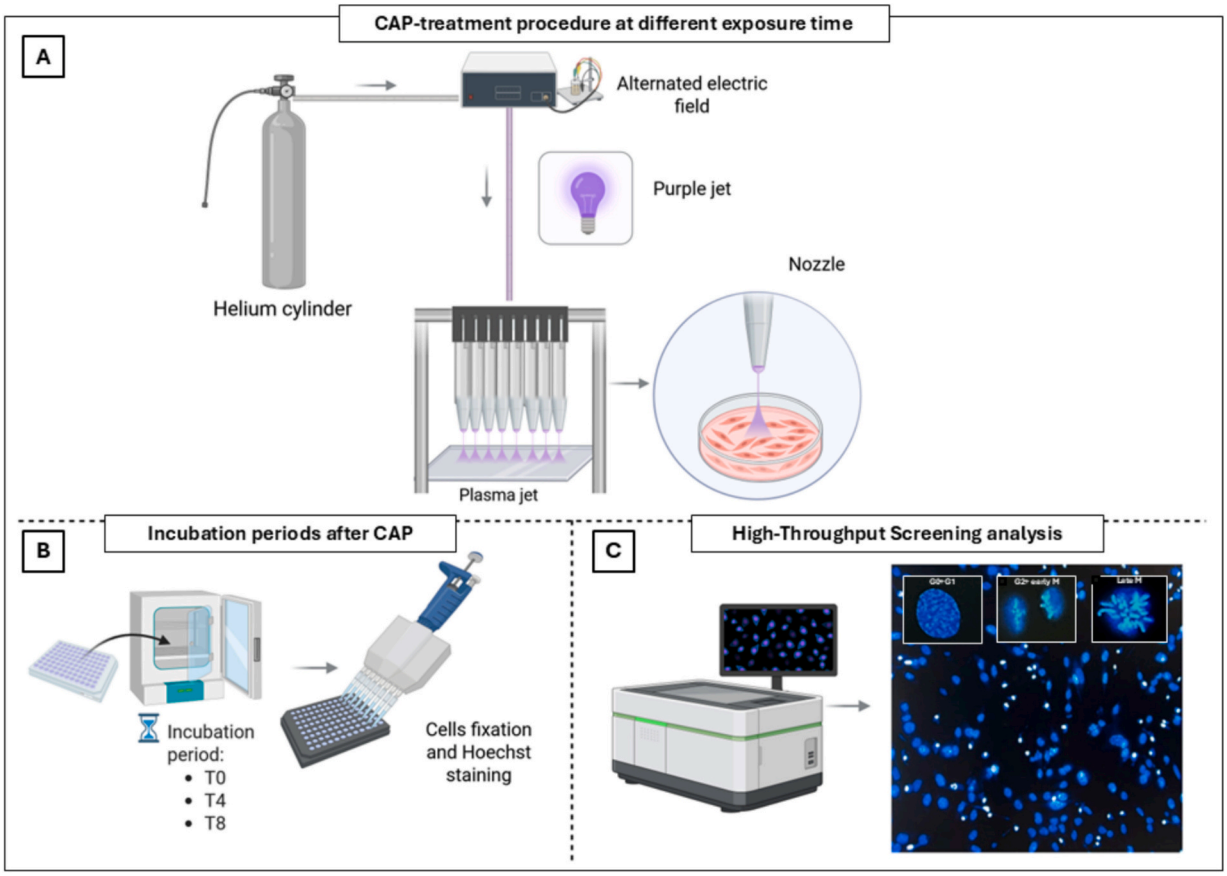

Fig. 3. A, Schematic of the CAP treatment applied to *Tursiops truncatus* skin cells. Helium gas was ionized by an alternating electric field to produce a plasma jet directed onto cultured cells. B, After CAP exposure, cells were incubated for 0, 4, or 8 h, fixed with 4% PFA, and stained with Hoechst 33342 to visualize nuclei. C, Representative image from the Operetta CLS high-content analysis system used for nuclear morphometric measurements. Based on these parameters, nuclei were classified into cell cycle groups (G0 + G1, S, and mitotic) and into additional groups: Small (nuclear fragments), Large (senescent nuclei), and collapsed cell nuclei.

2.5. High-throughput screening analysis

The Hoechst 33342 signal was detected using a dedicated filter combination (excitation: 360–400 nm; emission: 410–480 nm), with an exposure time of 10 ms, power to 15% and height set to 15% and − 5.0, respectively. A 20× air objective with an NA of 0.4 was used in non-confocal mode. Image acquisition and analysis were performed using Harmony® High-Content Imaging and Analysis Software (version 5.2, Revvity®, USA), in combination with the machine-learning-based PhenoLOGIC™ machine learning algorithm. This workflow enabled automated segmentation and quantification of nuclei based on Hoechst 33342 fluorescence and nuclear morphology. First, cell nuclei were identified using the 'Find Nuclei' building block applied to the Hoechst 33342 fluorescence channel. The segmentation parameters were then optimized to accurately identify individual nuclei while separating closely spaced nuclei and minimizing background signal and artefacts. In the second step, the mean nuclear Hoechst fluorescence intensity (Intensity) and the nuclear parameters nuclear width (Width), nuclear length (Length), were quantified. The nuclei with non-specific or low-intensity signals were removed using a thresholding strategy. A minimum of 17 fields per well was acquired to score enough objects for each tested condition. The number of nuclei counted for each well ranged from 2000 (at incubation time T0 h) from 9000 (at incubation time T8).

2.6. Cell nuclei counting and clustering methodology

The nuclear parameters measured in the cell nuclei included Hoechst intensity (Intensity), nuclear width (Width), nuclear length (Length), and the circularity of the nuclear shape (Ratio), defined as 1/(nuclear length/nuclear width). The parameter Ratio serves as an inverse aspect ratio metric. Values approaching 1 indicate a circular morphology, or nuclear roundness, while lower values reflect increasingly elongated or irregular nuclear shapes. The ratio was used as a morphological descriptor to evaluate changes in nuclear shape under experimental conditions.

Regarding the parameter Intensity, since the fluorescence intensity of Hoechst-stained nuclei is directly proportional to DNA content, it was used as a proxy to determine the cell cycle phase of individual cells. In addition, several cellular processes can be inferred from the analysis of nuclear morphometric features such as Hoechst intensity or parameters including nuclear width and nuclear length. Based on these principles, we developed a morphology-based quantitative methodology to determine the proportion of cells in different mitotic stages, as well as those exhibiting senescence-like morphology or apoptosis-like morphology, within an in vitro cell population (Fig. 4).

Once trained, the model automatically classified the entire nuclear population according to the defined phenotypes.

Combining mathematically the values of the parameter Length, Ratio and Intensity, all cell nuclei were clustered within defined groups (Table1). This procedure allowed to define seven groups named respectively: G0 + G1 (nuclei in G0 and G1 phase), S (nuclei in DNA-Synthesis phase), G2 + early-M (nuclei in G2 and early-Mitotic phase), late-M (nuclei in late-Mitotic phase), Small (small nuclear fragments with condensed chromatin and highest Intensity), Large (large nuclei), Collapsed-phenotype (nuclei with condensed chromatin), see (Table1). The cell nuclei number in each group was counted for each experimental

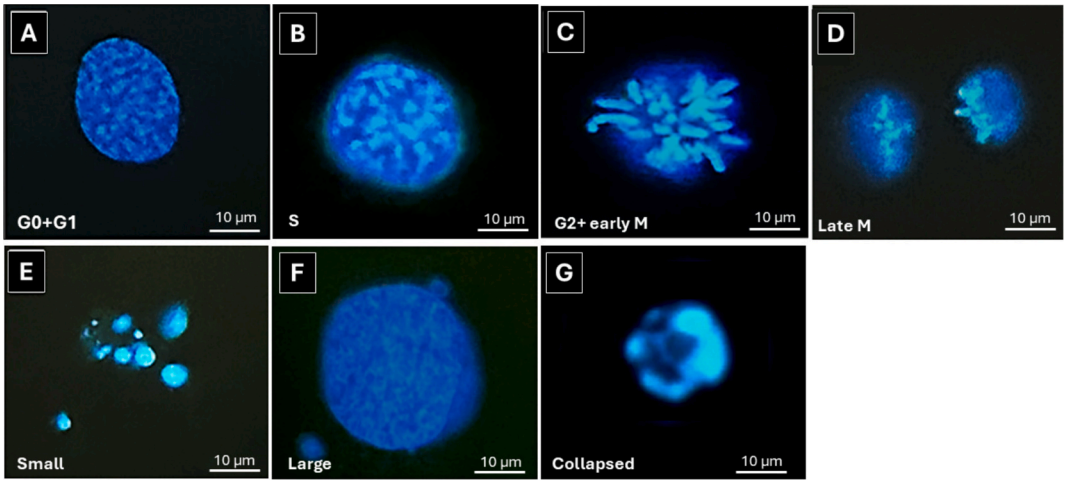

Fig. 4. Representative images showing cell nuclei clustering into the seven groups: **A**, cell nucleus in "G0 phase" showing a nucleus into a non-proliferating state of cells. **B**, cell nucleus in "S phase" representing the phase of DNA synthesis. **C**, cell nucleus in "M-early phase", showing a nucleus in the early mitotic phase in which the chromatin is condensed into visible chromosomes. **D**, cell nucleus in "M-late phase" showing a nucleus in the late mitosis in which the duplicated chromosomes are pulled apart by the mitotic spindle in the two sister cells. **E**, "Large" cell nucleus showing enlarged morphology with loose heterochromatin. **F**, "Small" showing small nuclear fragments and compacted chromatin. **G**, collapsed-phenotype nucleus showing condensed chromatin.

condition tested (CAP exposure time and incubation period), and data were compared to the control condition (untreated cells). To describe the CAP exposure time-effect we considered the average number of cell nuclei per experimental condition tested.

Classification pipeline: Segmentation: Cell nuclei were identified using the 'Find Nuclei' building block applied to the Hoechst 33342 fluorescence channel. Segmentation parameters were optimized to accurately identify each individual nucleus, separate closely spaced nuclei, and minimize background signal and artefacts. Feature extraction: For each segmented nucleus, the following parameters were quantified: Intensity: mean nuclear Hoechst fluorescence intensity, reflecting chromatin condensation state; Length and Width: nuclear morphometric descriptors reflecting size and shape. Nuclei with non-specific or low-intensity signals were removed using a thresholding strategy to ensure data quality. A minimum of 17 fields per well was acquired to score a sufficient number of objects per condition. As output, a CSV file containing millions of information on cell nuclei was automatically generated per each plate analyzed. Classification strategy:

MANUAL VALIDATION STEP; for each plate analyzed under the different experimental conditions, we manually examined 50 nuclei per cell cycle phase, evaluating both the images and the corresponding nuclear parameters. Categories included nuclei in G0 phase, nuclei in S phase (DNA synthesis), mitotic nuclei (including metaphase and sister cells), small nuclear fragments, large nuclei with low intensity resembling senescent-phenotype cells, and collapsed-phenotype nuclei. Nuclear parameters intensity, length, and inverse aspect ratio, were used to define threshold ranges (see Table 1).

THRESHOLD SETTING PROCESS; Manually established thresholds, based on direct observation, were then applied to all CSV files in each nucleus. Nuclei resulted clustered into seven biologically defined groups through a mathematical combination of Length, Intensity as illustrated in the matrix plot (Fig. 7): G0 + G1: low Intensity, rounded/ellipsoid shape, S phase: intermediate-to-high Intensity (onset of DNA duplication),

G2 + early-M: high Intensity (condensed chromosomes), Late-M (sister cells): small size, high Intensity (still-condensed DNA post-division), Large nuclei: large size, low Intensity (senescence-associated morphology), Small fragments: small size (nuclear fragmentation), Collapsed-phenotype nuclei: very high Intensity, condensed chromatin, no fragmentation. Nuclei with a collapsed phenotype exhibited intensity values reflecting extreme chromatin condensation (see Table 1). Notably, these nuclei showed markedly higher intensity thresholds (22,000–50,000), whereas all other nuclear groups consistently displayed values below 22,000. Accordingly, distinct threshold ranges were applied to classify nuclei in M phase, collapsed-phenotype nuclei, and nuclear fragments.

Validation: The classification output was validated against the MTT viability assay, showing consistent results across all experimental conditions (T0, T4, T8) and CAP exposure times:

At T0, nuclear counts were not significantly different from control, consistent with MTT results. At T4 and T8, significant reductions in nuclear counts following 10-min CAP exposure aligned with the significant decrease in cell viability detected by the MTT assay.

To confirm the reliability of this approach, two independent operators manually verified, in each experimental replicate and across hundreds of cells, that the nuclei automatically classified by the model were correctly assigned to their respective nuclear group, by directly observing the nuclei and their corresponding parameter values. Additionally, the proliferation marker Ki-67 was used to o support the classification of nuclei in the mitotic phases.

2.7. *Cell cycle profiling of Tursiops truncatus fibroblasts*

To determine the cell cycle profile of the Normal population after plasma treatment, the frequency of cell nuclei within specific Hoechst arbitrary fluorescence intensity unit ranges was measured and plotted: 2000–9000 arbitrary fluorescence intensity units for nuclei in the G0 + G1 phase, 9000–12,000 for nuclei in the S phase, and 12,000–22,000 for nuclei in the early and late M phases. Nuclear parameter assessment was performed using automated image analysis (Harmony® High-Content Imaging and Analysis Software with PhenoLOGIC™ algorithm, Revvity®, USA, version 5.2).

The validation of the specific thresholds for the parameters (Intensity, Size, and Ratio) used to define the clustering range for nuclei was performed by manually verifying the values of each individual nucleus in the images obtained from Harmony image analysis (over one hundred cell nuclei per condition tested were analyzed).

The nuclear morphology and condensation have been proposed as a tool to provide a screening of normal, senescent and apoptotic cells (Filippi-Chiela et al., 2012; Schorpp et al., 2016; Otero-Sabio et al., 2022). Considering these studies, our method, which combines three key morphometric parameters (length, intensity, and InvAR) to classify nuclei, effectively differentiates cells into G0/G1, S-phase, and G2/M groups, thus allowing us to accurately track cell cycle phases.

2.8. Immunofluorescence analysis

Immunofluorescence analysis was performed to identify apoptotic cells and proliferative fibroblasts. The total cell population was characterized using an anti-β-actin antibody. Cells were fixed with 4% paraformaldehyde for 15 min at room temperature. Following fixation, cells were gently washed twice with PBS for 5 min each to completely remove the paraformaldehyde, and then permeabilized with 0.1% Triton X-100 for 10 min at room temperature. After permeabilization, cells were washed twice with PBS to remove residuals.

Subsequently, cells were treated with 5% BSA in PBS 1× for 30 min to block endogenous nonspecific sites and then incubated overnight at 4 °C with the following primary antibodies: anti-β-actin mouse 1:500 (Sigma-Aldrich, St. Louis, MO, USA); anti-Caspase-3 rabbit 1:500 (Millipore, Burlington, MA, USA); anti-Ki67rabbit 1:200 (Antibodies Online, Aachen, Germany). After primary antibody incubations, additional washing steps (3 steps × 5 min with PBS) were performed.

Cells were then incubated for 2 h with the secondary antibodies Alexa Fluor 488 (Invitrogen, Waltham, MA, USA goat anti-mouse IgG (H + L), Cat# A32733, dilution 1:500) and Alexa Fluor Plus 647 (Invitrogen, Waltham, MA, USA, goat anti-rabbit IgG (H + L), Cat# A32733, dilution 1:500). To ensure species specificity and the absence of cross-reactivity between the two secondary antibodies, we performed an Immunofluorescence analysis in which both secondary antibodies (Alexa Fluor 488 and 647) were applied simultaneously, but only one primary antibody was used. Confocal microscopy analysis confirmed the absence of cross-reactivity and validated the species specificity of the antibodies (data not showed). After secondary antibody incubations, additional washing steps (3 steps × 5 min with PBS) were performed.

Nuclei were stained with Hoechst 33342 (Sigma-Aldrich, St. Louis, MO, USA, dilution 1:10000). Negative controls were performed by substituting primary antibodies with bovine serum albumin in PBS. For each experimental condition, 3 randomly selected fields from 4 wells, per plate were analyzed. Cells were analyzed using the confocal microscope (Leica TCS SP5).

The β-actin staining delineated cell boundaries more clearly, which facilitated the identification of individual cells, especially in areas where nuclei were clustered or overlapping. This was particularly beneficial in dense cultures, where cytoplasmic staining helped to distinguish neighboring cells, reducing the probability of double-counting or omitting cells. In addition, β-actin staining provided morphological context, enabling confirmation of cell integrity and overall health.

All immunofluorescence and histological evaluations, including assessment of β-actin, caspase-3, Ki-67, and nuclear morphology, were performed by an observer blinded to the CAP treatment conditions. This approach was implemented to reduce bias in the qualitative description of cellular morphology and staining patterns.

2.9. Statistical methodology

A parametric negative binomial generalized linear mixed model was used for the data analysis. This seems an appropriate choice, since it extends the Poisson model by accounting for overdispersion.

The design model includes two variables, namely plasma exposure time (Exptime) and incubation time (Inctime), which correspond to the duration of plasma treatment and the time cells spend in the incubator after treatment and before analysis. Both variables are treated as categorical to account for potential nonlinear effects and their interaction.

Furthermore, the plate-specific effect is modelled as a random intercept. One model is fitted for the counts in each group, and a further model is fitted for the overall counts (i.e. the sum of all group counts). After fitting the model, pairwise comparisons of the control sample (i.e. Exptime = 0 and Inctime) with all other Exptime levels are corrected for multiple comparisons using the Dunnett method. The analysis was performed using the R software (R Core Team, 2024) and the lmerTest (Kuznetsova et al., 2017) and emmeans (Lenth, 2024) packages.

3. Results

3.1. The Tursiops truncatus skin-derived cell line

The *Tursiops truncatus* skin-derived cells maintained in culture exhibited high viability and adhered readily to the culture substrate, forming a confluent monolayer composed of randomly oriented, spindle-shaped cells a morphology consistent with fibroblasts (Fig. 5). These phenotypic characteristics were consistently observed across all independent experimental replicates. In a previous study, we conducted Immunofluorescence characterization of this cell line, which confirmed the fibroblastic identity based on the expression of specific fibroblast markers (Otero-Sabio et al., 2022).

3.2. MTT-assay results on cell viability

The MTT assay did not display significant variations on *Tursiops truncatus* fibroblasts cell viability after CAP-treatment at 1, 2 5 and 10 min, at the incubation period of 0 h, when compared to the control condition (Fig. 6A). No significant changes in cell viability were observed after short-time CAP exposure (1, 2 and 5 min) at 4-h post treatment. A significant decrease in cell viability was detected after long-time CAP exposure (10 min) at 4-h post treatment ($p = 0.003$) (Fig. 6B). No significant changes in cell viability were observed after short-time CAP exposure (1, 2 and 5 min), at 8- h post treatment. A significant decrease in cell viability was observed after long-time CAP exposure (10 min), at 8- h post treatment ($p = 0.042$) (Fig. 6C). The incubation of cells with Thapsigargin (positive control) at the highest concentration tested (4 μM) significantly reduced cell viability, if compared to the control condition at 0-h ($p = 0.007$), 4-h ($p = 0.001$) and 8-h ($p < 0.001$) post treatment. No significant changes in cell viability were detected at the lower concentrations of Thapsigargin tested (0.4 μM, 0.04 μM, 0.004 μM, and 0.0004 μM) at any incubation period, if compared to the control condition (Fig. 6 and Table 2 and 3 in the Supplementary Material).

3.3. High-content screening viability versus MTT viability assay

To validate the MTT viability assay, we performed an alternative viability test by quantifying cell nuclei under each experimental condition (short- and long-time CAP exposure at incubation periods of 0, 4, and 8 h post-treatment), using high-content screening and comparing the results to the control condition.

At the 0-h incubation period post-treatment, nuclear counts were not significantly different from the control, consistent with the MTT assay results (see Table 1, Supplementary Material).

At the 4-h incubation period post-treatment, nuclear counts were significantly reduced compared to the control, aligning with the MTT assay results that demonstrated a significant decrease in cell viability following 10 min of CAP exposure (see Table 1, Supplementary Material).

At the 8-h incubation period post-treatment, nuclear counts were significantly reduced compared to the control, aligning with the MTT assay results that demonstrated a significant decrease in cell viability following 10 min of CAP exposure (see Table 1, Supplementary Material).

3.4. Cell nuclei classification and clustering

Then, nuclei are classified and clustered based on the mathematical combination of some parameters. Specifically, Length, Intensity and InvAR, which were plotted in the matrix plot showing the distribution of the nuclear population in the seven groups (Fig. 7). The nuclei in the G0 + G1 group, show decondensed chromatin and low values of Intensity, rounded or ellipsoid shape (Fig. 7A). Cell nucleus in S phase show higher intensity values, due to the starting of the DNA duplication phase

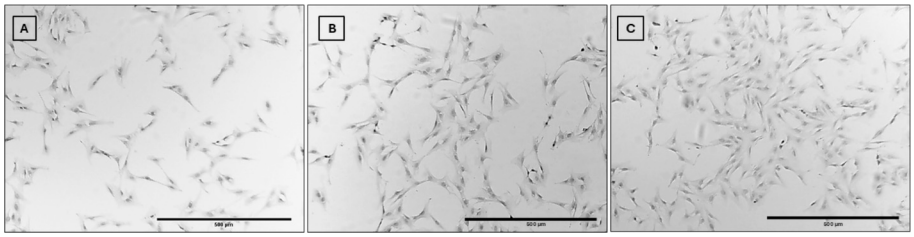

Fig. 5. Phase-contrast images showing the morphological development of *Tursiops truncatus* skin-derived cells. **A.** Fibroblasts seeded at 1×10^4 cells/mL in standard serum-rich medium (10% FBS), imaged after 24 h in culture. This condition represents the incubation time T0. **B.** Image of fibroblasts in culture at the condition incubation time T4. **C.** Image of fibroblasts in culture at the incubation time T8.

(Fig. 7B). The cells in G2 + early-Mitotic phase show high Intensity values due to the formation of the highly condensed chromosomes (prophase and metaphase) (Fig. 7C). The cells in the late-Mitotic phase, are named sister cells and show small nuclear size and high Intensity due to the still condensed DNA (Fig. 7D). The cells showing large size of the nucleus and low Intensity value, typical of the senescent cells, were clustered in the Large group (Fig. 7E). The small nuclear fragments showing small size were clustered in the Small group (Fig. 7F). The cells showing nuclei with condensed chromatin and very high Intensity values (Table 1), were clustered as "collapsed-phenotype cell nuclei" (Fig. 7G).

3.5. Cell nuclei quantification at T0, T4 and T8 after CAP treatments

To assess cellular responses following CAP treatment, the number of cell nuclei was quantified under each experimental condition, which included short-times exposure (1, 2, and 5 min) and a long-time exposure (10 min). The results, shown in the line graph (Fig. 8), represent cell nuclei counts at three post-treatment incubation periods: T0, T4, and T8. Overall, a general trend of decreasing cell count was observed with increasing exposure time, with the most pronounced reduction occurring after the 5-min exposure. Interestingly, at the 10-min exposure condition, cell nuclei count converge across all incubation periods, suggesting a uniform cytotoxic effect regardless of post-treatment time. However, it is important to note the variability observed between replicates. This heterogeneity, particularly at shorter exposure times (1, 2 and 5 min), suggests non-linear responses among samples, which may reflect biological variability or differential sensitivity to CAP. Moreover, the absence of a progressive dose-dependent reduction in nuclei count at these shorter exposure times points to a possible threshold effect rather than a linear cytotoxic response.

This non-linearity may be due to the complex interplay of reactive species and cellular defense mechanisms, which could buffer mild CAP-induced stress before a critical damage threshold is reached.

3.6. Results of CAP treatment per nuclei group at the incubation period T0

The results of the statistical analysis at incubation time T0, performed separately for each nuclear category, are presented in Fig. 9. Overall, the data reveal biologically meaningful, exposure-dependent shifts in nuclear populations immediately following CAP treatment, indicating rapid modulation of both cell cycle dynamics and cellular physiology.

At T0, short CAP exposures (1, 2, and 5 min) did not produce significant changes in the G0 + G1 group, suggesting that brief plasma treatment does not acutely affect cells in quiescent or early interphase states. In contrast, long CAP exposure (10 min) was associated with a significant reduction in this population ($p = 0.036$), consistent with an early departure from quiescence or the onset of cellular stress under sustained treatment conditions.

Proliferative cell cycle phases exhibited coordinated responses to short CAP exposures. Specifically, the number of S-phase nuclei increased significantly after 1 min of CAP treatment ($p = 0.004$), while the G2 + early-M group showed a significant increase at the same exposure duration ($p < 0.001$). In addition, the Late-M group displayed significant increases following 1, 2, and 5 min of CAP exposure ($p = 0.035$, $p = 0.004$, and $p < 0.001$, respectively). Taken together, these concurrent changes across successive cell cycle phases indicate a rapid and transient stimulation of cell cycle progression, rather than isolated or random fluctuations within individual nuclear categories.

In contrast, nuclear populations associated with cellular stress or damage showed more pronounced responses at longer exposure times. The Large nuclei group exhibited a significant reduction after 10 min of CAP treatment ($p < 0.001$), a change that may reflect early nuclear condensation or shrinkage. No significant changes were observed in the Small fragments group across any exposure condition, suggesting that overt nuclear fragmentation is not a dominant immediate response at T0.

Notably, the collapsed-phenotype cell nuclei group showed significant increases following short CAP exposures of 1, 2, and 5 min ($p < 0.001$, $p < 0.001$, and $p = 0.003$, respectively), indicating that degenerative nuclear changes can emerge early, even under conditions that simultaneously promote proliferative signals in other cell subpopulations (see Fig. 9). Overall, the findings at T0 describe a duration-dependent cellular response to CAP exposure, characterized by the coexistence of early cell cycle activation and initial stress-associated nuclear alterations, underscoring the biological complexity of CAP-induced effects at early post-treatment stages.

3.7. Results of CAP treatment per nuclei group after the incubation period T4

The inferential analysis at T4 revealed statistically significant and biologically relevant alterations in multiple nuclear populations following CAP exposure (Fig. 10), indicating sustained effects on cell cycle organization and nuclear integrity.

A pronounced reduction in the G0 + G1 nuclear population was observed after 10 min of CAP exposure ($p < 0.001$), reflecting a marked depletion of quiescent or early interphase cells. This shift suggests a disruption of normal cell cycle homeostasis, potentially associated with cell cycle arrest, exit from the proliferative pool, or progression toward degenerative states. Consistent with this interpretation, the number of nuclei classified as collapsed-phenotype increased significantly after 5 and 10 min of CAP treatment ($p = 0.019$ and $p < 0.001$, respectively), supporting the view that prolonged exposure is associated with progressive nuclear damage.

At the same time, significant increases were detected in nuclei assigned to the S, G2 + early-M, and Late-M groups at longer exposure durations, particularly after 10 min of CAP treatment (all $p < 0.001$). While these increases may initially suggest accumulation of cells in proliferative phases, their occurrence in parallel with declining G0 + G1 and increasing collapsed-phenotype nuclei indicates that they more likely reflect impaired cell cycle progression, such as checkpoint activation or incomplete mitotic transit, rather than productive

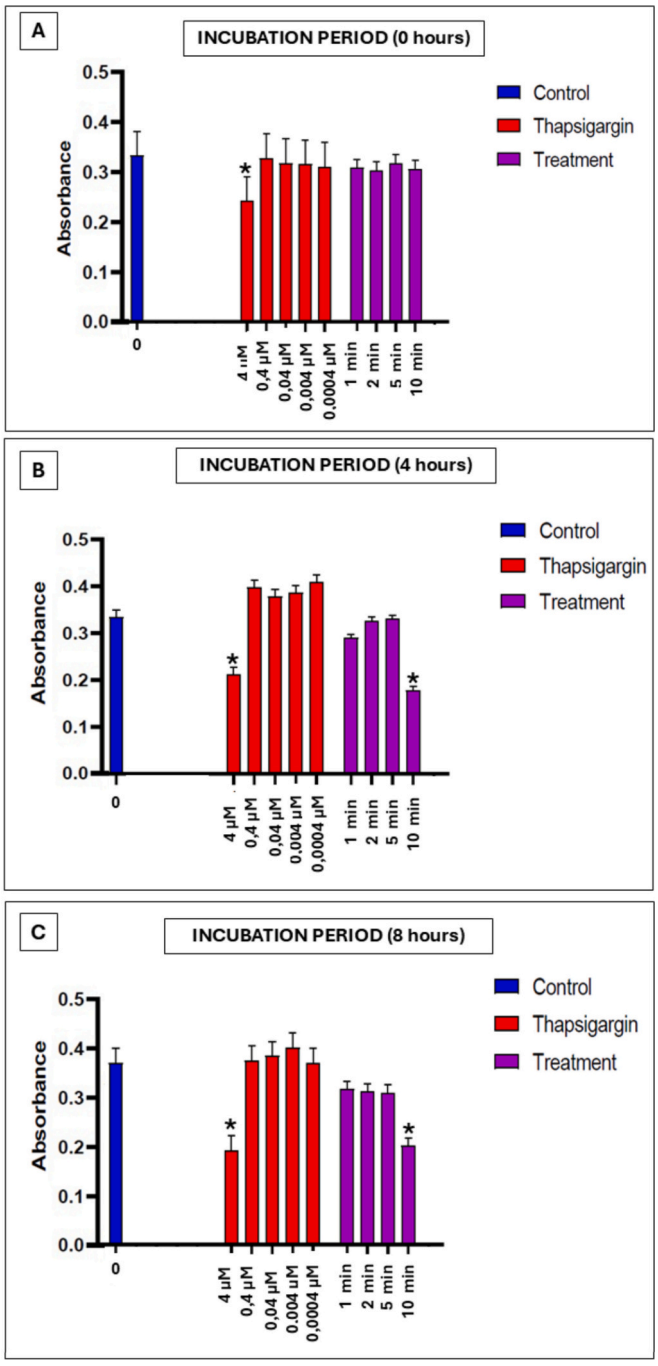

Fig. 6. Histograms showing MTT assay results following short- (1, 2, 5 min) and long-time (10 min) CAP treatments compared with Thapsigargin positive control (red). The X-axis indicates Thapsigargin concentrations (4–0.0004 µM) and CAP exposure times; the Y-axis shows raw absorbance values. Panels represent incubation times of (A) 0 h (T0), (B) 4 h (T4), and (C) 8 h (T8) post-treatment. Data are expressed as mean ± SD from three independent experiments. Data were normalized to the control for the statistical analysis presented in Tables 2 and 3 (Supplementary Material). Asterix (*) indicate statistically significant experimental conditions (p-value <0.05). (For interpretation of the references to colour in this figure legend, the reader is referred to the web version of this article.)

proliferation.

The Large nuclei population also showed a significant reduction following 10 min of CAP exposure ($p < 0.001$), a change consistent with the loss of metabolically active cells and further supporting a shift toward cellular stress or death-associated outcomes.

Taken together, the T4 data reveal a duration-dependent reorganization of nuclear phenotypes, in which prolonged CAP exposure is associated with depletion of quiescent cells, accumulation of aberrant or arrested cell cycle states, and increased nuclear collapse. This pattern is indicative of a threshold-like response, whereby extended CAP treatment disrupts cell cycle regulation and compromises nuclear integrity, highlighting the biological limits of CAP exposure in this cellular model.

3.8. *Results of CAP treatment per nuclei group after the incubation period T8*

The results of the statistical analysis of the T8 dataset are presented in Fig. 11, which reports the analyses performed separately for each nuclear class. Overall, the data indicate exposure-time–dependent alterations in nuclear distributions, reflecting sustained effects of CAP on cell cycle regulation and nuclear integrity at this later incubation time.

Indeed, at T8, short CAP exposures did not produce significant changes in the G0 + G1 nuclear population. In contrast, a marked reduction in G0 + G1 nuclei was observed after 10 min of CAP exposure ($p < 0.001$), indicating a depletion of quiescent or early interphase cells. This shift suggests a disruption of cell cycle homeostasis, potentially reflecting exit from G0/G1 or a transition toward stress-associated cellular states, including growth arrest or cell death.

In the G2 + early-M group, a significant decrease was also detected following 10 min of CAP treatment ($p < 0.001$), pointing to an impaired entry into mitosis. Such alterations are consistent with the accumulation of oxidative or genotoxic stress, which is known to interfere with mitotic progression. In contrast, the Late-M population exhibited a significant increase after 10 min of exposure ($p < 0.001$), suggesting a delay or arrest during late mitotic stages. This redistribution across mitotic phases indicates that prolonged CAP exposure affects not only cell cycle entry but also successful completion of mitosis.

Morphological nuclear alterations became more prominent at longer exposure times. The number of Large nuclei group showed a significant decrease after 10 min of CAP exposure ($p < 0.001$), in line with the lower amount of nuclei displaying morphologies typical of metabolically active or senescent cells. Conversely, the Small fragments group exhibited a significant increase after 10 min ($p < 0.001$), indicating the presence of nuclear fragmentation, a feature commonly associated with advanced cellular damage and cell death–related processes.

The collapsed-phenotype cell nuclei group displayed a biphasic response. A significant decrease was observed after 2 and 5 min of CAP exposure ($p = 0.041$ and $p = 0.038$, respectively), followed by a pronounced increase after 10 min ($p < 0.001$). This pattern suggests that short exposures may be associated with transient cellular adaptation or recovery processes. At variance, prolonged CAP treatment overwhelms cellular protective mechanisms, resulting in widespread nuclear collapse.

Taken together, the T8 dataset reveals a complex, time-dependent response to CAP exposure. Short treatment durations are associated with limited or adaptive nuclear changes, whereas prolonged exposure leads to extensive disruption of cell cycle progression, accumulation of mitotic abnormalities, and increased nuclear fragmentation and collapse. The concurrent decrease in the Large nuclei population and increase in damage-associated nuclear classes following 10 min of CAP exposure suggest a shift toward irreversible cellular stress and death-related outcomes. While the reduction in nuclei with senescence-like morphology may indicate altered senescence dynamics, this interpretation remains speculative and warrants further investigation using dedicated senescence markers.

3.9. *Immunofluorescence results*

Immunofluorescence analysis was performed in *Tursiops truncatus* skin fibroblasts to obtain an additional, qualitative, analysis of cellular morphology. The total cell population was identified using an anti-

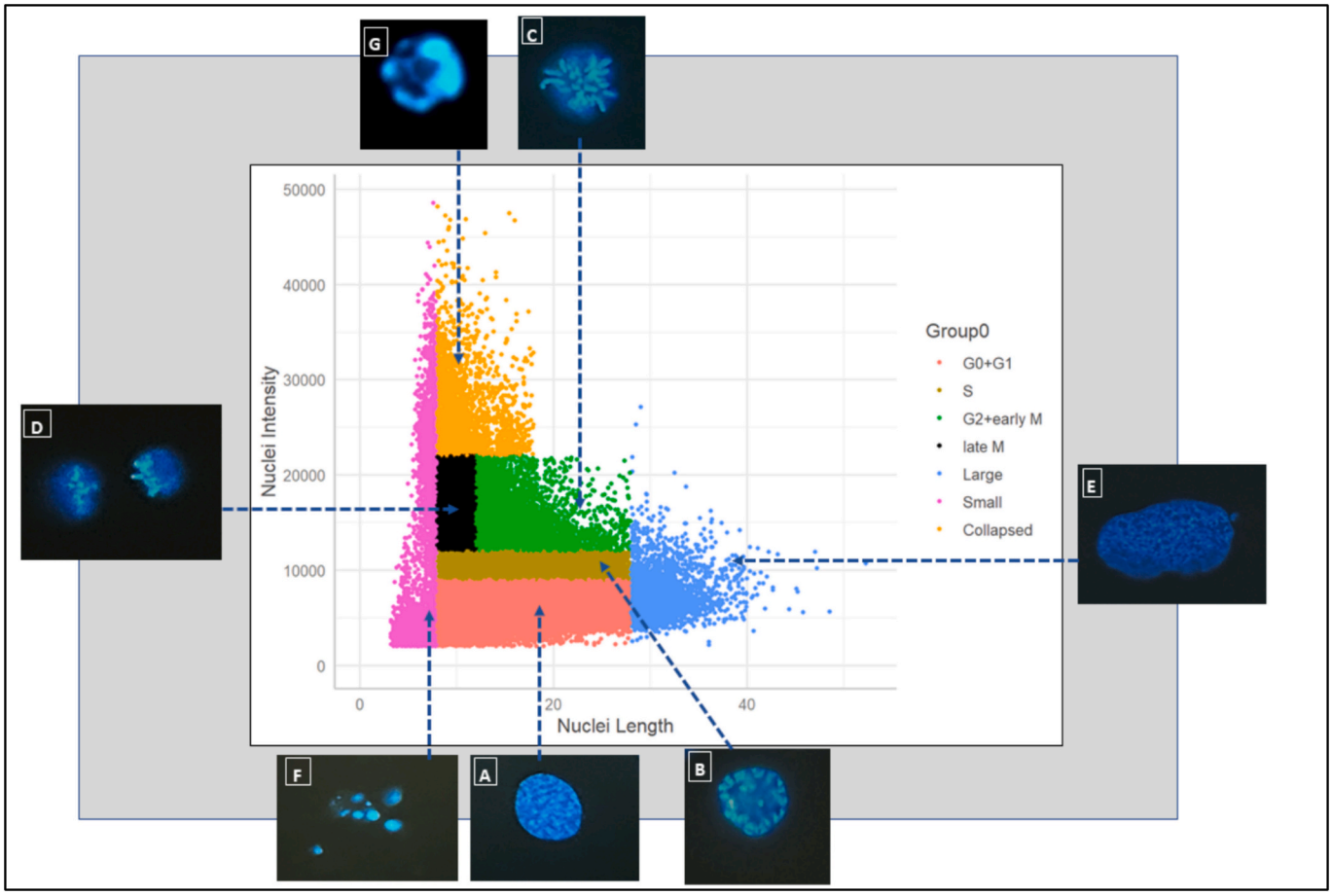

Fig. 7. Matrix plot showing nuclear classification derived from the combination of Length, Intensity, and InvAR parameters. **A**, image of a cell nucleus in the G0 + G1 phase. **B**, image of a cell nucleus during the DNA-Synthesis phase. **C**, image of a cell nucleus in the G2 + early Mitotic phase, note the condensed chromosomes. **D**, example of a cell nucleus in the late mitotic phase, after division into two sister cells, note the still condensed DNA starting to decondense. **E**, example of a Large nucleus showing low intensity value and large size. **F**, nuclear fragments, chromatin condensation and fragmentation; **G**, collapsed-phenotype nucleus, condensed chromatin, high intensity, no DNA fragmentation.

β-actin antibody. All cells exhibited β-actin immunoreactivity (β-actin-ir), with staining outlining the typical filamentous cytoskeletal pattern (Figs. 12B and 13B). To provide further insights on the eventual activation of the pro-apoptotic cascade, we used Caspase3 antibody. A small population of cells displayed Caspase-3 immunoreactivity, showing an ellipsoid or rounded shape. Caspase-3 was observed mostly in the cytoplasm. Although the active form can enter the nucleus, the predominant immunoreactivity appeared perinuclear in many cells (Fig. 12 E, F, G and Fig. 13 E, F, G).

To further characterize our cell populations, Ki-67, a marker of cell proliferation typically localized in the nucleus during the active phases of the cell cycle, was also immunostained. These experiments revealed the presence of cells undergoing mitosis under all the experimental conditions tested. Ki-67 immunoreactivity (Ki-67-ir) was localized in the nuclei of fibroblasts (Fig. 14) which were in active phases of the cell cycle (G1, S, G2, and mitosis). Although these observations cannot be used to infer specific proliferative activity of our cell models, they support the results obtained with the formerly described approaches and reported in Fig. 9,10,11.

3.10. The collapsed-phenotype cell nuclei group are not caspase-3 immunoreactive

The cell nuclei clustering analysis, based on the mathematical integration of parameters Length, Intensity, and InvAR, identified a distinct subset of nuclei, which we named the "Collapsed Cell Nuclei Group." This group exhibited the highest Hoechst intensity values (22000–50,000) and nucleus lengths ranging from 8 to 18 μm (Table 1).

Collapsed-phenotype cells appear rounded, and sometimes exhibit an irregular shape, resulting from the loss of cytoskeletal integrity, with collapsed β-actin filaments leading to altered cell morphology (Fig. 15). The nuclei appear shrunken, with condensed chromatin (Fig. 15B, C, D, E, F). Furthermore, Immunofluorescence analysis revealed that collapsed cells were immunoreactive to β-actin but negative for Caspase-3 (Fig. 15A).

Although these observations cannot be used to imply specific functional states or mechanisms, which are not the aim of this article and will request future, in depth investigations, they are provided here to qualitatively support the experimental evidence reported in Figs. 15.

4. Discussion

This study investigates the effects of CAP exposure on skin fibroblasts derived from the cetacean *Tursiops truncatus*, with the aim of evaluating its potential relevance for future therapeutic applications in the treatment of skin lesions. To assess CAP-associated changes in cell cycle dynamics and early cellular responses, fibroblasts were exposed to short CAP treatments (1, 2, and 5 min) and a longer treatment (10 min), allowing comparison across different exposure durations.

Incubation times of 0, 4, and 8 h following CAP exposure were selected to capture both early and delayed cellular responses. The 0-h time point enabled evaluation of immediate effects on the fibroblast

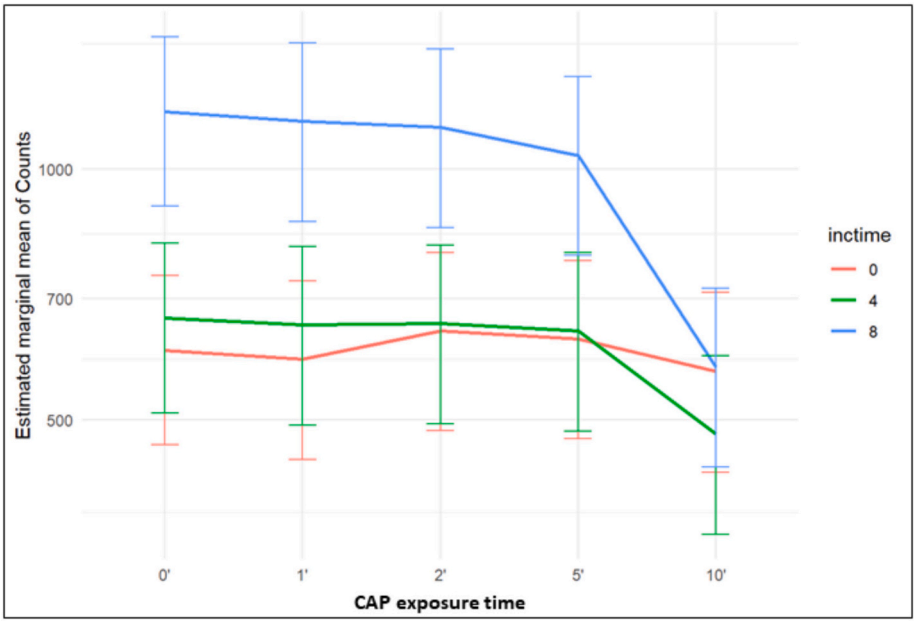

Fig. 8. Line graph showing the trend of the average of the cell nuclei counting after the short-time (1, 2 and 5 min.) and long-time (10 min.) of CAP exposure after the incubation period 0, 4 and 8 h following the CAP treatments. On the x-axis are represented the exposure time (0, 1, 2, 5, 10 min). On the y-axis are reported the average of nuclei counting. The bars represent the error bar. Each line colour (red, green, blue) corresponds to the incubation time considered (0, 4, 8 h) respectively. The lines for each colour represent the mean of the three independent experiments. The (exposure time 0) represents the control condition. (For interpretation of the references to colour in this figure legend, the reader is referred to the web version of this article.)

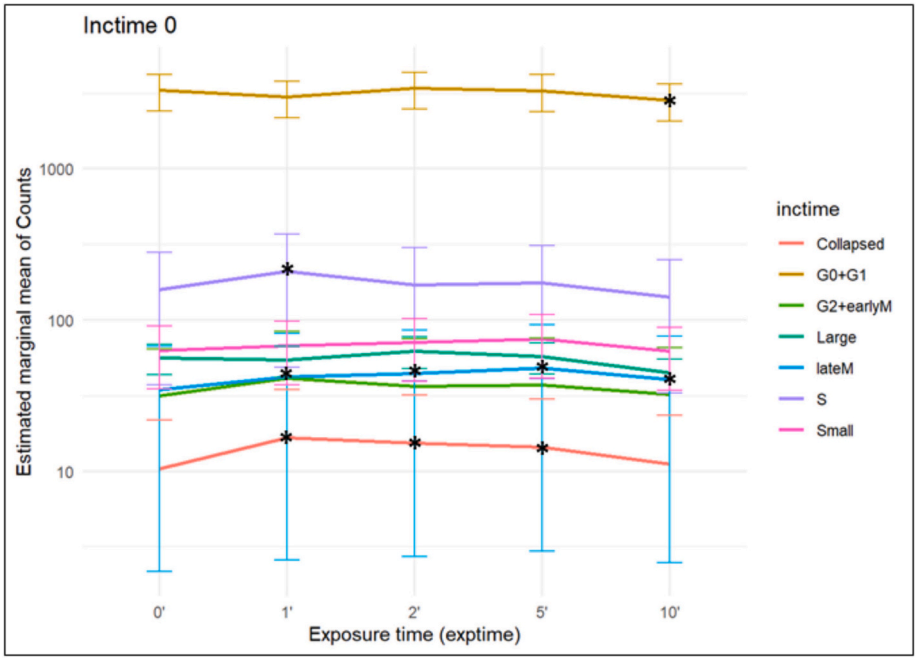

Fig. 9. Line graph showing the impact of short- (1, 2, 5 min) and long-time (10 min) CAP exposure on different nuclear groups. Colored dots represent the mean nucleus counts per group, and error bars indicate standard error. Asterisks denote statistically significant changes. Contrasts are performed by Wald tests with Dunnet correction. Key findings include: G0 + G1 nuclei decreased after 10 min ($p = 0.036$); S phase increased after 1 min ($p = 0.004$); G2 + early-M increased after 1 min ($p < 0.001$); Late-M increased after 1, 2, and 5 min ($p = 0.035, 0.004, < 0.001$); Large nuclei decreased after 10 min ($p < 0.001$); Collapsed-phenotype nuclei increased after 1, 2, and 5 min ($p < 0.001, < 0.001, 0.003$).

population present at the time of treatment, including acute changes in proliferation-related parameters or cytotoxicity.

The 4- and 8-h time points were included to assess early delayed responses within the same treated cell population. Given the typical fibroblast doubling time (approximately 16–72 h), these time points are not suitable for detecting measurable cell proliferation. Instead, they provide insight into early CAP-induced effects, such as modulation of metabolic activity, cell cycle distribution, adhesion, and nuclear morphology. Longer incubation times (24–72 h) were not considered, as cell division during this interval would introduce newly generated, untreated cells, potentially confounding attribution of observed effects specifically to CAP exposure This design choice therefore reduced

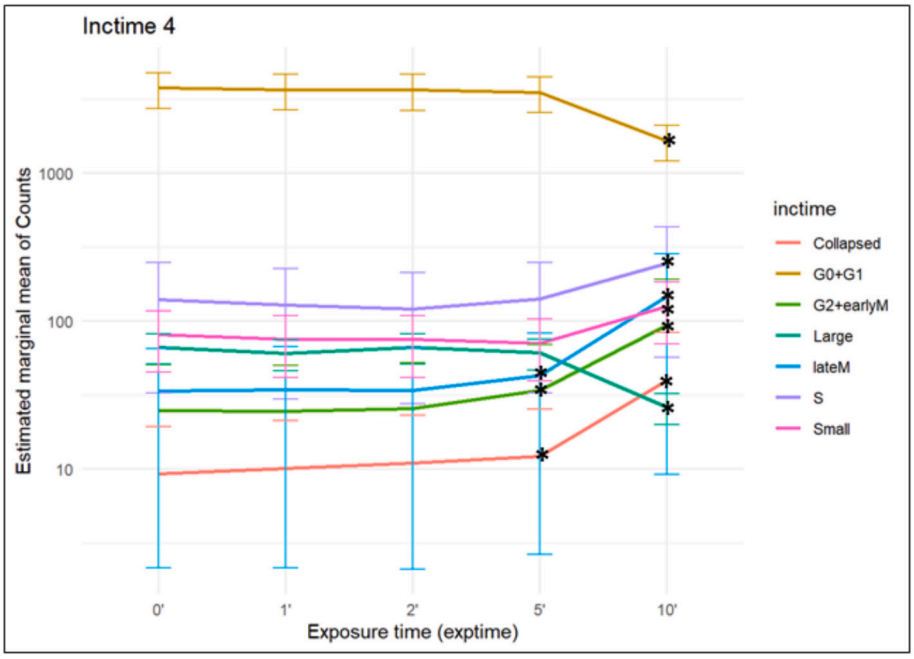

Fig. 10. Line graph showing the impact of short- (1, 2, 5 min) and long-time (10 min) CAP exposure on different nuclear groups. Colored dots indicate mean nucleus counts per group, and error bars show standard error. Asterisks denote statistically significant changes. Contrasts are performed by Wald tests with Dunnet correction. Key findings: G0 + G1 nuclei decreased after 10 min ($p < 0.001$); Collapsed-phenotype nuclei increased after 5 and 10 min ($p = 0.019, < 0.001$); S, G2 + early-M, and Late-M groups increased after 10 min ($p < 0.001$); Large nuclei decreased after 10 min ($p < 0.001$).

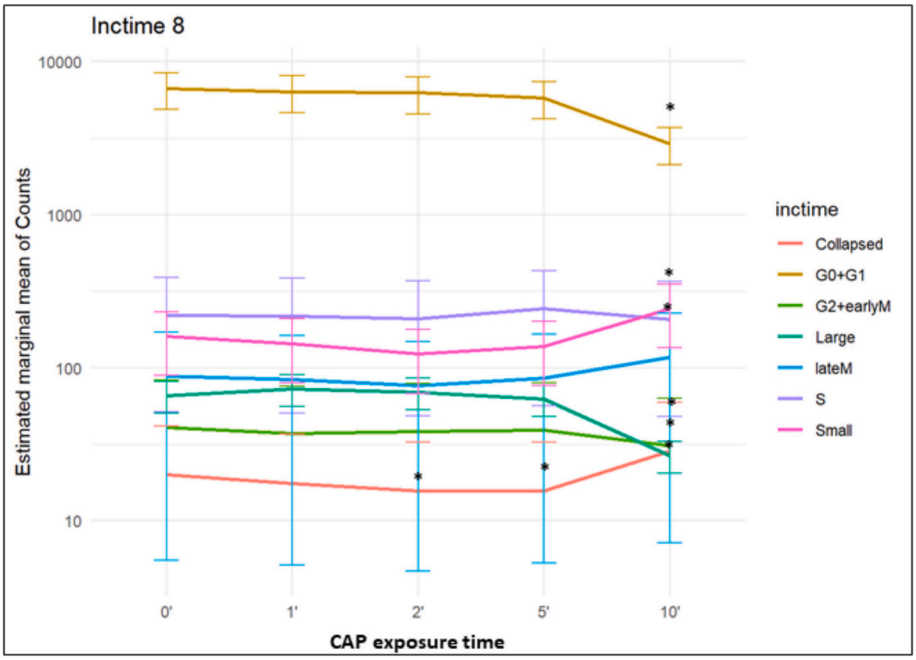

Fig. 11. Line graph showing the impact of short- (1, 2, 5 min) and long-time (10 min) CAP exposure on different nuclear groups. Colored dots indicate mean nucleus counts per group, with error bars representing standard error. Asterisks denote statistically significant changes. Contrasts are performed by Wald tests with Dunnet correction. Key observations: G0 + G1 and G2 + early-M nuclei decreased after 10 min ($p < 0.001$); Late-M increased after 10 min ($p < 0.001$); Large nuclei decreased and Small fragments increased after 10 min ($p < 0.001$); Collapsed-phenotype nuclei showed transient decreases after 2 and 5 min ($p = 0.041, 0.038$).

variability and improved interpretability of treatment-associated early responses.

Across the experimental conditions, no clear linear dose–response relationship was detected among CAP-treated groups. Instead, the data showed non-monotonic patterns across exposure times, a result consistent with previous findings in plasma medicine, where CAP-induced biological responses frequently exhibit non-linear or biphasic behavior (Kazemi, 2024). Such non-linearity reflects the multifactorial nature of CAP; whose biological activity arises from the combined and time-dependent effects of reactive oxygen and nitrogen species (RONS) and electric fields. Similar response patterns have been reported in human fibroblasts; where transient alterations in redox balance modulated

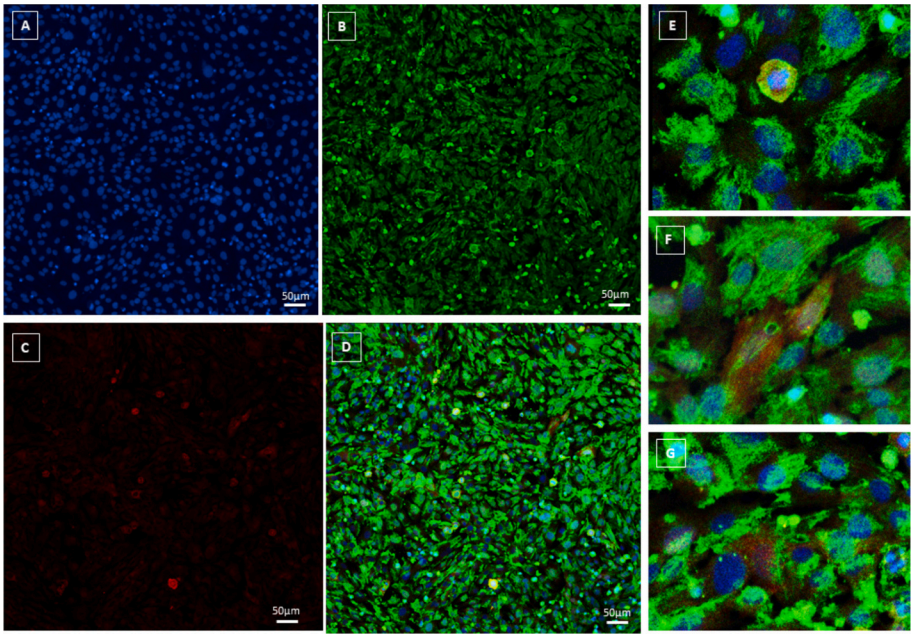

Fig. 12. Images of bottlenose dolphin skin-derived fibroblasts showing the immunoreactive cells to the antibodies β-actin and Caspase-3 respectively after 1 min of CAP treatment and 8 h of incubation period. Cell nuclei are labeled by Hoechst dye. **A.** Image of Hoechst stained nuclei. **B.** Image of β-actin stained cells. **C.** Image of Caspase-3 stained cells. **D.** Merge showing the colocalization of the Caspase-3, β-actin and Hoechst. **E., F., G.** Details showing the caspase-positive cells during the apoptotic process, (Caspase-3 in red, β-actin in green and Hoechst in blue). (For interpretation of the references to colour in this figure legend, the reader is referred to the web version of this article.)

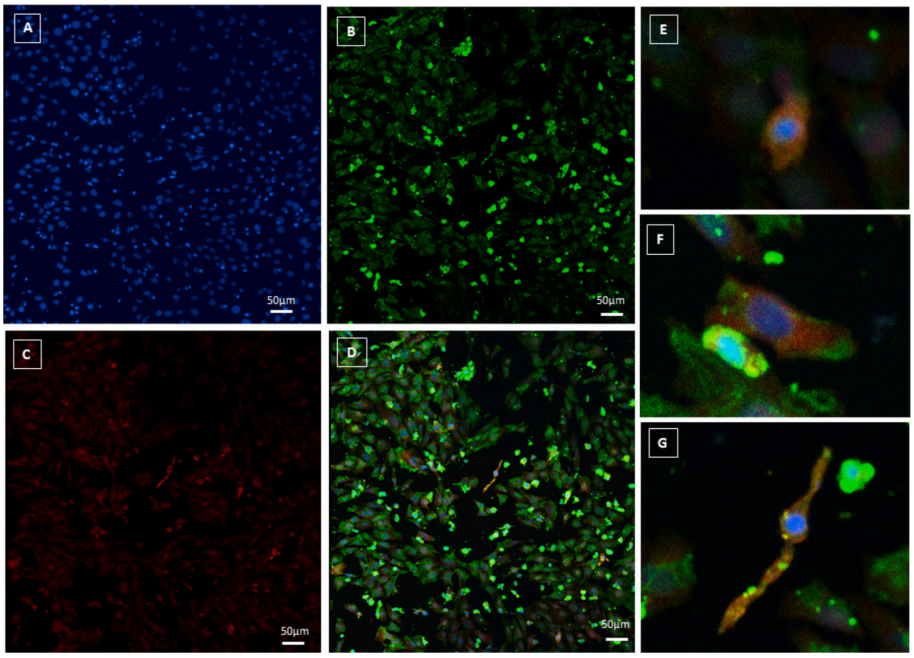

Fig. 13. Images of bottlenose dolphin skin-derived fibroblasts showing the immunoreactive cells to the antibodies β-actin and Caspase-3 respectively after 10 min of CAP treatment and 8 h of incubation period. Cell nuclei are labeled by Hoechst dye. **A**. Image of Hoechst stained nuclei. **B.** Image of β-actin stained cells. **C.** Image of Caspase-3 stained cells. **D.** Merge showing the colocalization of the Caspase-3, β-actin and Hoechst. In **E.**, **F.**, **G.** Details showing the caspase-positive cells during the apoptotic process, (Caspase-3 in red, β-actin in green and Hoechst in blue). (For interpretation of the references to colour in this figure legend, the reader is referred to the web version of this article.)

CAP-associated cytotoxicity despite continued exposure (Virard et al., 2015).

Overall, the results of the present study indicate a biphasic response pattern to CAP exposure. Short treatment durations were associated with a relative increase in nuclei classified in S, G2, and M phases, consistent with enhanced cell cycle progression at early time points. In contrast, longer exposure was associated with reductions in G0/G1 and Large nuclei populations and an increase in collapsed-phenotype cell nuclei, indicating a shift toward cytotoxic outcomes. These statistically supported trends align with previous reports describing threshold-dependent CAP effects in eukaryotic cells, where treatment duration and intensity critically influence cellular outcomes (Motain et al., 2021;

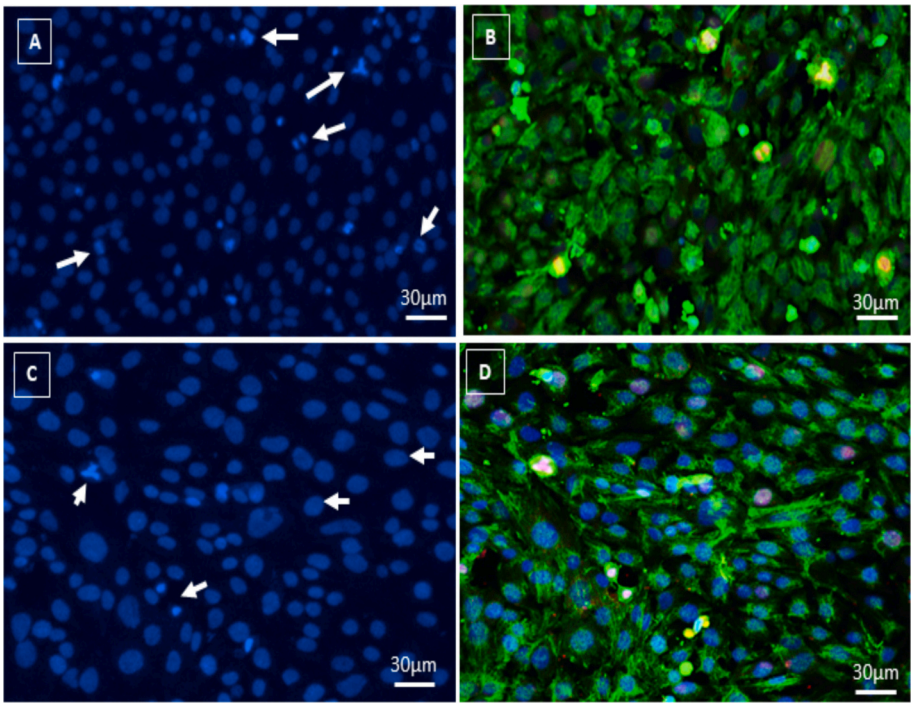

Fig. 14. Images of bottlenose dolphin skin-derived fibroblasts showing the immunoreactive cells to the antibodies Ki-67, β-actin and Hoechst respectively. **A.** Image showing Hoechst stained nuclei (nuclei in mitotic phases are indicated by white arrows), after 1 min of CAP exposure and 8 h of incubation period. **B.** the Ki67, β-actin and Hoechst colocalization in the same field of image A (magenta cells, are the mitotic cells labeled with white arrows in A). **C.** Image showing Hoechst stained nuclei (nuclei in mitotic phases are indicated by white arrows), after 10 min of CAP exposure and 8 h of incubation period. **D.** The Ki67, β-actin and Hoechst colocalization in the same field of C (magenta cells, are the mitotic cells labeled with white arrows in C). (For interpretation of the references to colour in this figure legend, the reader is referred to the web version of this article.)

Bai et al., 2025).

While the present data do not establish a mechanistic explanation, the observed exposure-dependent patterns are compatible with models in which moderate CAP exposure promotes early pro-survival or activation responses, whereas prolonged exposure leads to cellular damage. Such behavior has been attributed in prior studies to the accumulation of reactive species beyond cellular buffering capacity (Kaushik et al., 2014; Babajani et al., 2024), although direct measurements of these processes were beyond the scope of this work.

4.1. Differential effects of short- and long-time CAP exposure on fibroblast cell cycle distribution

In this study, nuclear morphology of fibroblasts was analyzed at three post-treatment time points (T0, T4, T8) following CAP exposure. Short CAP exposure was associated with changes proportion of S-phase and G2 + early-M nuclei at T0 and T4, accompanied by a decrease in G0 + G1 nuclei, indicating a transient acceleration of the cell cycle (Kim and Chung, 2016; Zhai et al., 2022). These observations indicate a shift in nuclear distribution profiles over time.

By contrast, prolonged CAP exposure (10 min) led to an accumulation of collapsed-phenotype nuclei at T8, reflecting delayed cytotoxic effects rather than immediate apoptosis (Dubuc et al., 2018; Bhartiya et al., 2022). The absence of caspase-3 immunoreactivity in these nuclei suggests that cell death processes may involve non-apoptotic pathways; however, no mechanistic conclusions can be drawn based on the present data (Fiaschi et al., 2006; Kreuz and Fischle, 2016). Overall, these findings highlight a time-dependent response of fibroblasts to CAP, characterized by changes in nuclear distribution patterns following short exposure and the appearance of morphologically distinct collapsed nuclei after prolonged exposure.

4.2. Cell nuclei clustering enabled analysis of the effects of CAP treatment

Cell nuclei were classified according to the mitotic phase (G0 + G1, S, G2 + early-Mitosis, and late-Mitosis) to analyze the effects of CAP exposure. Nuclear morphology naturally changes during mitosis and in other processes, such as apoptosis or senescence (Narita et al., 2003). Chromatin condensation and decondensation occur during normal cell cycle progression (Filippi-Chiela et al., 2012); and alterations such as nuclear fragmentation; enlargement; or irregularity have been associated with chemical stress and disruptions in cell cycle regulation (Vakifahmetoglu et al., 2008). Recent approaches allow tracking of individual cell cycle phases alongside cellular features; including protein localization and organelle morphology (Roukos et al., 2015).

In our study, Ki-67-positive nuclei were observed in cells classified as S and G2 + early-M, consistent with their proliferative status and with the increased frequency of these subgroups following short-time CAP exposure. In contrast, Ki-67 immunoreactivity was not detected in nuclei from the G0 + G1 and collapsed-phenotype groups within the analyzed samples, suggesting that these populations may represent non-proliferative or terminal states such as quiescence, senescence, or cell death. However, these observations are based on qualitative assessment and were not supported by quantitative analysis.

β-Actin staining revealed disrupted actin filaments specifically in cells with collapsed nuclei, indicating that cytoskeletal destabilization may be a hallmark of the cell death mechanism induced upon long-time CAP exposure.

4.3. Reduced cell viability after long-time CAP treatment: advantages and limitations of the MTT assay

Using the MTT assay, we observed a statistically significant reduction in cell viability following long-time CAP exposure in bottlenose dolphin skin fibroblasts. The MTT colorimetric assay is based on the

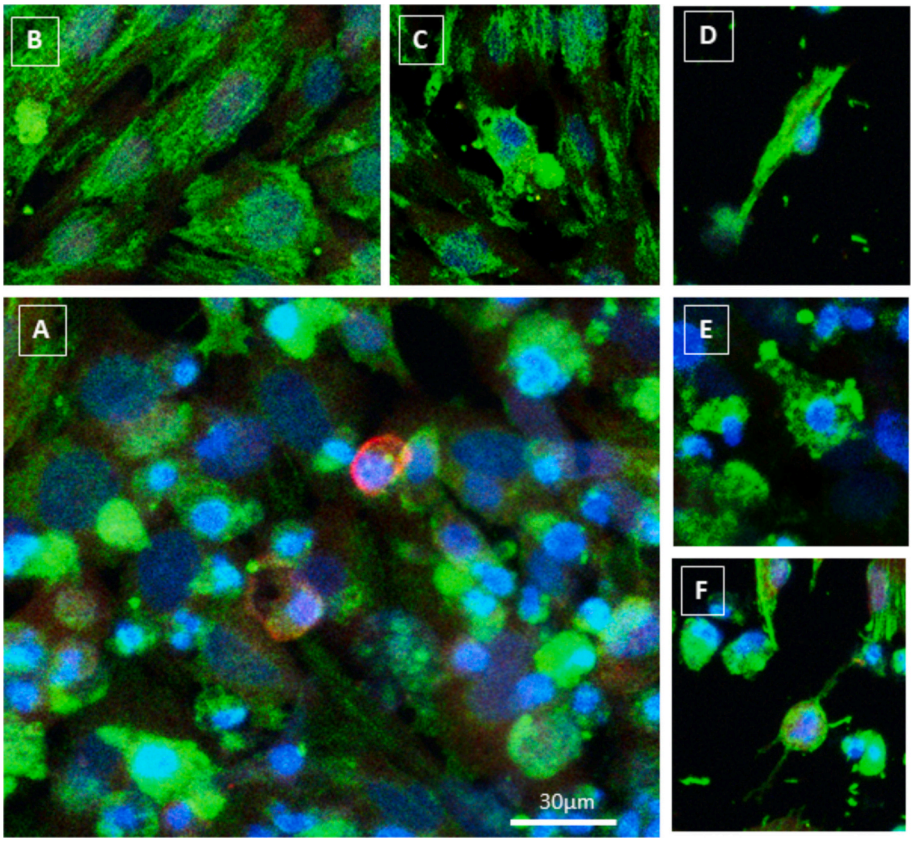

Fig. 15. Images showing the β-actin and caspase-3 immunoreactivity in the fibroblasts after 10 min of CAP exposure and 8 h of incubation. **A.** Merged image showing the apoptotic cells positive to the Caspase-3 (in red), β-actin (in green). The Hoechst stained nuclei are showed in blue. **B.** Detail of β-actin immunostained fibroblasts, showing the typical filamentous distribution and organization of actin in the cytoskeleton. **C.** Detailed view of a β-actin immunoreactive fibroblast shows actin filaments initiating depolymerization within the cell. **D.** a detailed view of a fibroblast shows condensed β-actin filaments in the cytoskeleton, resulting in altered cell shape, with the nucleus labeled in blue. **E.** A fibroblast is shown with actin filaments arranged along the cell membrane, forming external vesicles that deform the cell shape. **F.** details of collapsed-phenotype cells reveal a typical rounded shape, condensed chromatin, and high nuclear intensity values. (For interpretation of the references to colour in this figure legend, the reader is referred to the web version of this article.)

reduction of the tetrazolium salt MTT into an insoluble purple formazan product by metabolically active cells, therefore it is commonly considered as a method to assess cell viability.

Cell viability was consistently lower in the long-exposure groups compared with controls and short-time CAP treatments, indicating an exposure-dependent decrease in metabolic activity. These results suggest that prolonged CAP treatment is associated with reduced cellular viability under the experimental conditions tested.

Our observations are consistent with previous reports in other mammalian models. In murine and rat fibroblasts, extended CAP exposure has been associated with a significant reduction in cell viability, which has been attributed to increased oxidative burden during prolonged treatment (Wu et al., 2023). Similarly; studies in human fibroblasts have reported decreased MTT-derived viability following long CAP exposure; consistent with impaired metabolic activity and cellular stress (Bhartiya et al., 2022).

However, interpretation of MTT-based viability data in the context of CAP exposure requires caution. CAP-generated reactive oxygen and nitrogen species (RONS) can directly interact with tetrazolium salts or their formazan products, potentially altering absorbance values independently of true changes in cell number or viability (Bao et al., 2016). Such chemical interference may lead to either overestimation or underestimation of viable cells in CAP-treated samples.

In addition, the MTT assay provides a population-level measure of metabolic activity and does not resolve heterogeneity within the cell population. Because the assay integrates signals from cells at different stages of the cell cycle and physiological states, it cannot distinguish whether observed changes reflect altered metabolic activity, cell cycle arrest, or cell loss within specific subpopulations. Consequently, MTT results alone are insufficient to draw detailed conclusions regarding cell cycle–dependent responses to CAP treatment.

To address these limitations and strengthen the interpretation of the viability data, we complemented the MTT assay with high-content imaging. This approach allows single-cell–level quantitative analysis, enabling discrimination among cell cycle phases, assessment of proliferation-related features, and detection of morphological alterations. The combined use of metabolic and imaging-based analyses provides a more robust and nuanced evaluation of CAP-induced cellular responses.

4.4. Collapsed-phenotype fibroblasts: a form of cell death induced by CAP exposure

In this study, we identified a distinct nuclear phenotype, here referred to as “collapsed-phenotype nuclei”, characterized by condensed chromatin, reduced nuclear size, altered cell morphology, and disruption of β-actin filament organization. Exposure to CAP increased the number of collapsed nuclei at all treatment times analyzed; however, after 8 h of incubation, this increase persisted only following the 10-min CAP exposure. In contrast, shorter exposure times were associated with a reduction in the number of collapsed-phenotype nuclei at the same time point. These observations indicate a time- and exposure-dependent pattern in the occurrence of this nuclear phenotype. Cells displaying collapsed-phenotype nuclei exhibited shrunken morphology, chromatin

condensation, and disrupted actin filament organization, as observed by β-actin staining.

Although apoptosis is a well-characterized form of regulated cell death typically associated with caspase activation and nuclear fragmentation (Budihardjo et al., 1999), the absence of caspase-3 staining in these cells suggests that the observed phenotype does not align straightforwardly with the classical caspase-dependent apoptotic pathway. However, the lack of caspase-3 immunoreactivity alone is not sufficient to exclude apoptosis, as caspase activation can be transient or occur outside the temporal window analyzed, and caspase-independent apoptotic pathways have also been described. Therefore, the nature of the observed cell death should be interpreted with caution.

The combination of morphological features observed in the present cell model namely chromatin condensation, cytoskeletal alterations, and changes in cellular integrity partially overlap with morphological characteristics reported in association with different forms of cellular stress and cell death. However, in the absence of functional and molecular evidence, these similarities should be interpreted as descriptive resemblances rather than indicators of specific cellular processes. Previous studies have reported that CAP exposure can be associated with multiple cellular outcomes, including apoptosis, necrosis, pyroptosis, and ferroptosis, particularly in cancer models (Bekeschus et al., 2017). Moreover; CAP responses appear to be highly cell-type dependent. For instance; some tumor cell lines exhibit relative resistance to CAP-induced cytotoxicity; requiring specific exposure conditions to elicit measurable effects (Bekeschus et al., 2017). These findings highlight the variability of CAP-associated cellular responses and support cautious interpretation when extrapolating results across different cell types and experimental systems. It is well documented that CAP treatment can lead to the accumulation of reactive oxygen and nitrogen species (RONS) in the extracellular environment (Bao et al., 2016); and that oxidative conditions are often associated with alterations in cytoskeletal organization and chromatin structure (Balta et al., 2021; Turrini et al., 2017; Kreuz and Fischle, 2016). However, no direct measurements of oxidative stress, signaling pathway activation, or functional outcomes were performed in the present study, and therefore no mechanistic conclusions can be drawn, as these analyses were beyond the scope of this work.

Taken together, our exploratory datasets describe a reproducible nuclear and cellular phenotype associated with CAP exposure in bottlenose dolphin skin fibroblasts. The cellular processes underlying these observations cannot be defined based on morphological features alone. Further studies incorporating additional molecular and functional approaches will be necessary to better characterize the observed phenotype and its biological basis.

4.5. Cetacean fibroblasts exhibit unique sensitivity and stress-response mechanisms to CAP

Our results indicate that dolphin fibroblasts display a distinct response to CAP exposure, characterized by time- and dose-dependent changes in nuclear morphology and cytoskeletal organization. These observations suggest that cetacean cells may respond differently to oxidative stress conditions compared with other mammalian cell types commonly reported in the literature, although direct comparative data are not available.

In this context, it is relevant that cetaceans have evolved specific adaptations in pathways involved in oxidative stress regulation and DNA repair, which may contribute to modulating cellular responses under conditions of increased reactive oxygen species, such as those generated by CAP (Peruffo et al., 2025). During cetacean evolution; genetic modifications affecting stress-response pathways have been described; including the loss of MAP3K19; which has been associated with altered susceptibility to oxidative stress–induced inflammation; and the absence of POLM; a low-fidelity DNA polymerase potentially involved in error-prone repair processes (Poirier, 2021).

Furthermore, enhanced DNA repair capacity and genome stability have been reported in cetacean fibroblasts, including in bowhead whale models, together with the expression of stress-associated protective factors such as CIRBP (Firsanov et al., 2025). These features may provide a biological context for the cellular phenotypes observed in the present study under CAP-induced oxidative conditions.

4.6. Limitations in the nuclear classification approach

Although nuclear size, shape, and integrity can reflect major cellular processes such as proliferation, mitosis, and cell death, these parameters are inherently indirect and may not capture the full complexity of cellular responses particularly under non-physiological conditions such as exposure to CAP. CAP induces a variety of stress responses primarily mediated by RONS species, which can affect multiple cellular compartments, signaling pathways, and death mechanisms simultaneously. These effects may result in atypical or overlapping nuclear phenotypes that are not easily categorized into classical stages of the cell cycle or standard apoptotic morphology. For instance, oxidative stress may cause nuclear condensation, fragmentation, or swelling that mimic features of late mitosis or apoptosis, without necessarily reflecting canonical cell cycle progression. Thus, while our nuclear classification offers useful insight into CAP's impact on nuclear architecture and population-level shifts in nuclear features, it should be interpreted with caution and viewed as complementary to molecular markers (e.g., Ki-67, caspase-3) rather than a standalone method for physiological inference.

4.7. Plasma dosimetry

An important and debated issue in plasma medicine is the actual exposure level of active agents generated by plasma treatment. Even restricting to what is commonly considered to be the main agent, that is reactive oxygen and nitrogen species (thus neglecting the possible action of electric field, charged species and electromagnetic radiation), a proper assessment requires the measurement of the concentration of several different species, a task which was not possible in the present case. We can however provide an estimate by comparing with more detailed studies on this topic performed using similar devices. For example, it is possible to measure the production of reactive species in water treated by a plasma jet. This was done by Uchida et al. using a plasma jet similar to the present one. They observed a large difference depending if the plasma plume was or not in contact with the water surface. In the case of plasma contact, using pure helium as process gas, 75 μmol/L of H_2O_2, 22 μmol/L of NO_2^- and 12.5 μmol/L of NO_3^- were detected after irradiating 3 mL of water for 5 min (Uchida et al., 2016). It is, however, not so straightforward to derive from concentrations in water samples the actual production rate in the gas phase, as Henry's law and chemical processes taking place in the liquid phase are involved. Furthermore, it is not easy to detect short-lived species, which may play an important role in biological processes. In this respect, an interesting contribution was given by Tresp et al., who measured using EPR spectroscopy the absolute values for OH and O_2^- radical concentration and their production rate in phosphate-buffered saline solution treated with a radiofrequency plasma jet operating in argon, showing a production rate of the order of 100 pmol/s for the OH radical and more than twice for the O_2^- anion (Tresp et al., 2013). A review of concentrations of chemical species in samples of water and other liquids treated with plasma jets shows a good degree of variability; probably related to the specific details of the different devices used in the experiments (Khlyustova et al., 2019), and suggests as a rough estimate for our case a concentration of the order of 10 μmol/L of H_2O_2, and similar for NO_2^-.

It is important to emphasize that RONS concentrations measured in water samples, or in simple buffered solutions, are only qualitatively representative of the RONS produced in the gas phase by the action of the energetic electrons of the plasma. Indeed, Henry's law coefficients, which determine the rate of migration of chemical species from the gas

to the liquid phase, can vary by orders of magnitude from one species to the other. Furthermore, reactions may occur in the liquid phase which would not occur in the gas phase. This is even more crucial when one tries to apply measurements performed in the gas phase or in water samples to complex media such as those used as nutrients for cell cultures. In the culture medium a wealth of new reactions can and will take place. Consequently, one should be aware that the results of other authors described above should be taken only as qualitative guidance, and not as a quantitative evaluation of the reactive species exposure associated with CAP treatment. Accordingly, observed effects should be interpreted in terms of exposure time–dependent responses rather than true dose–response relationships.

5. Conclusions

This observational study highlights time-dependent associations between CAP exposure and the cellular response of *Tursiops truncatus*-derived skin fibroblasts. Short exposure times (1, 2, and 5 min) were associated with higher proportions of nuclei in S, G2, and M phases, whereas prolonged exposure (10 min) was associated with reductions in G0 + G1 and Large nuclei, and increases in collapsed-phenotype and fragmented nuclei.

Although this exploratory dataset cannot be generalized to whole organisms or clinical applications without further validation, they provide a first example of standardized analysis of marine mammal cells responses to CAP under controlled experimental conditions.

Future studies to investigate CAP-induced molecular changes using complementary assays (e.g., transcriptomic or proteomic analyses) to explore responses in other cetacean-derived cell types are warranted.

CRediT authorship contribution statement

Alice Gonella: Methodology, Investigation, Data curation, Writing – original draft. **Leonardo Zampieri:** Validation, Methodology, Writing – original draft. **Livio Finos:** Supervision, Methodology, Data curation, Conceptualization, Writing – original draft. **Matteo Zuin:** Methodology, Conceptualization. **Anna Perazzi:** Methodology, Conceptualization, Writing – original draft. **Giuseppina Covello:** Methodology, Data curation, Conceptualization, Writing – original draft. **Marta Giacomello:** Methodology, Formal analysis, Conceptualization, Writing – original draft. **Cinzia Centelleghe:** Methodology, Data curation, Writing – original draft. **Emilio Martines:** Methodology, Investigation, Conceptualization, Writing – original draft. **Antonella Peruffo:** Supervision, Data curation, Conceptualization, Writing – review & editing, Writing – original draft.

Funding

This study was supported by a University of Padova Grant (BIRD 2022 #BIRD228257) to Antonella Peruffo.

Declaration of competing interest

The authors declare that they have no known competing financial interests or personal relationships that could have appeared to influence the work reported in this paper.

Appendix A. Supplementary data

Supplementary data to this article can be found online at https://doi.org/10.1016/j.rvsc.2026.106249.

Data availability

The data presented in this study are available on request from the corresponding author.

References

Arndt, S., Unger, P., Wacker, E., Shimizu, T., Heinlin, J., Li, Y.F., Thomas, H.M., Morfill, G.E., Zimmermann, J.L., Bosserhoff, A.K., Karrer, S., 2013. Cold atmospheric plasma (CAP) changes gene expression of key molecules of the wound healing machinery and improves wound healing in vitro and in vivo. PLoS One 8 (11), e79325. https://doi.org/10.1371/journal.pone.0079325.

Babajani, A., Eftekharinasab, A., Bekeschus, S., Mehdian, H., Vakhshiteh, F., Madjd, Z., 2024. Reactive oxygen species from non-thermal gas plasma (CAP): implication for targeting cancer stem cells. Cancer Cell Int. 24, 344. https://doi.org/10.1186/s12935-024-03523-x.

Bai, F., Jia, F., Zhou, M., Zhang, Y., Qi, Chen Q., Gao, M., Ning, X., Yan, Z., Liu, X., Kong, M.G., Xia, Yumin, 2025. Cold atmospheric plasma counteracts oxidative stress and promotes dermal papilla cell proliferation and hair regrowth. J. Phys. D. Appl. Phys. 58 (16). https://doi.org/10.1088/1361-6463/adbbff.

Balta, E., Kramer, J., Samstag, Y., 2021. Redox regulation of the actin cytoskeleton in cell migration and adhesion: on the way to a spatiotemporal view. Front. Cell Dev. Biol. 8, 618261. https://doi.org/10.3389/fcell.2020.618261.

Bao, P., Lu, X., He, M., Liu, D., 2016. Kinetic analysis of delivery of plasma reactive species into cells immersed in culture media. IEEE Trans. Plasma Sci. 44, 2673–2681.

Bekeschus, S., Bräutigam, L., Wende, K., Hanschmann, E.M., 2017. Oxidants and redox signaling: perspectives in cancer therapy, inflammation, and plasma medicine. Oxidative Med. Cell. Longev. 2017, 4020253. https://doi.org/10.1155/2017/4020253.

Bhartiya, P., Kaushik, N., Nguyen, L., Bekeschus, S., Masur, K., Weltmann, K., Kaushik, N., Choi, E., 2022. Periodic exposure of plasma-activated medium alters fibroblast cellular homoeostasis. Int. J. Mol. Sci. 23, 3120. https://doi.org/10.3390/ijms23063120.

Brun, P., Pathak, S., Castagliuolo, I., Palù, G., Brun, P., Zuin, M., Cavazzana, R., Martines, E., 2014. Helium generated cold plasma finely regulates activation of human fibroblast-like primary cells. PLoS One 9. https://doi.org/10.1371/journal.pone.0104397.

Budihardjo, I., Oliver, H., Lutter, M., Luo, X., Wang, X., 1999. Biochemical pathways of caspase activation during apoptosis. Annu. Rev. Cell Dev. Biol. 15, 269–290. https://doi.org/10.1146/annurev.cellbio.15.1.269.

Busco, G., Robert, E., Chettouh-Hammas, N., Pouvesle, J., Grillon, C., 2020. The emerging potential of cold atmospheric plasma in skin biology. Free Radic. Biol. Med. 161, 290–304. https://doi.org/10.1016/j.freeradbiomed.2020.10.004.

Chupradit, S., Widjaja, G., Radhi Majeed, B., Kuznetsova, M., Ansari, M., Suksatan, W., Turki Jalil, A., Ghazi Esfahani, B., 2023. Recent advances in cold atmospheric plasma (CAP) for breast cancer therapy. Cell Biol. Int. 47, 327–340. https://doi.org/10.1002/cbin.11939.

Dubuc, A., Monsarrat, P., Virard, F., Merbahi, N., Sarrette, J.P., Laurencin-Dalicieux, S., Cousty, S., 2018. Use of cold-atmospheric plasma in oncology: a concise systematic review. Ther. Adv. Med. Oncol. 10. https://doi.org/10.1177/1758835918786475.

Duignan, P.J., Stephens, N.S., Robb, K., 2020. Fresh water skin disease in dolphins: a case definition based on pathology and environmental factors in Australia. Sci. Rep. 10, 21979. https://doi.org/10.1038/s41598-020-78858-2.

Fiaschi, T., Cozzi, G., Raugei, G., Formigli, L., Ramponi, G., Chiarugi, P., 2006. Redox regulation of beta-actin during integrin-mediated cell adhesion. J. Biol. Chem. 281, 22983–22991. https://doi.org/10.1074/jbc.M603040200.

Filippi-Chiela, E.C., Oliveira, M.M., Jurkovski, B., Callegari-Jacques, S.M., da Silva, V.D., Lenz, G., 2012. Nuclear morphometric analysis (NMA): screening of senescence, apoptosis and nuclear irregularities. PLoS One 7. https://doi.org/10.1371/journal.pone.0042522.

Firsanov, D., Zacher, M., Tian, X., Sformo, T.L., Zhao, Y., Tombline, G., Lu, J.Y., Zheng, Z., Perelli, L., Gurreri, E., Zhang, L., Guo, J., Korotkov, A., Volobaev, V., Biashad, S.A., Zhang, Z., Heid, J., Maslov, A.Y., Sun, S., Wu, Z., Gigas, J., Hillpot, E. C., Martinez, J.C., Lee, M., Williams, A., Gilman, A., Hamilton, N., Strelkova, E., Haseljic, E., Patel, A., Straight, M.E., Miller, N., Ablaeva, J., Tam, L.M., Couderc, C., Hoopmann, M.R., Moritz, R.L., Fujii, S., Pelletier, A., Hayman, D.J., Liu, H., Cai, Y., Leung, A.K.L., Zhang, Z., Nelson, C.B., Abegglen, L.M., Schiffman, J.D., Gladyshev, V.N., Maley, C.C., Modesti, M., Genovese, G., Simons, M.J.P., Vijg, J., Seluanov, A., Gorbunova, V., 2025. Evidence for improved DNA repair in long-lived bowhead whale. Nature. https://doi.org/10.1038/s41586-025-09694-5.

Inano, S., Kimura, M., Iida, J., Arima, N., 2013. Combination therapy of voriconazole and terbinafine for disseminated fusariosis: case report and literature review. J. Infect. Chemother. 19 (6), 1173–1180. https://doi.org/10.1007/s10156-013-0594-9.

Kamio, T., Nojo, H., Kano, R., Murakami, M., Odani, Y., Kanda, K., Mori, T., Akune, Y., Kurita, M., Okada, A., Inoshima, Y., 2025. Successful treatment of fungal dermatitis in a bottlenose dolphin *Tursiops truncatus*. Microorganisms 13 (1), 106. https://doi.org/10.3390/microorganisms13010106.

Kamiya, T., Hara, H., Adachi, T., 2013. Effect of endoplasmic reticulum (ER) stress inducer thapsigargin on the expression of extracellular-superoxide dismutase in mouse 3T3-L1 adipocytes. J. Clin. Biochem. Nutr. 52 (2), 101–105. https://doi.org/10.3164/jcbn.12-46.

Kaushik, N.K., Kaushik, N., Park, D., Choi, E.H., 2014. Altered antioxidant system stimulates dielectric barrier discharge plasma-induced cell death for solid tumor cell treatment. PLoS One 9 (7), e103349. https://doi.org/10.1371/journal.pone.0103349.

Kazemi A, McKayla J. N, Sven G. B, Girish S. K, Sean D. K. 2024. Cold atmospheric plasma medicine: applications, challenges, and opportunities for predictive control. Plasma 7(1), 233–257; doi:https://doi.org/10.3390/plasma7010014.

Khlyustova, A., Labay, C., Machala, Z., Ginebra, M.-P., Canal, C., 2019. Important parameters in plasma jets for the production of RONS in liquids for plasma medicine:

a brief review. Front. Chem. Sci. Eng. 13, 238–252. https://doi.org/10.1007/s11705-019-1801-8.
Kim, S.J., Chung, T.H., 2016. Cold atmospheric plasma jet-generated RONS and their selective effects on normal and carcinoma cells. Sci. Rep. 6, 20332. https://doi.org/10.1038/srep20332.
Kreuz, S., Fischle, W., 2016. Oxidative stress signaling to chromatin in health and disease. Epigenomics 6, 843–862. https://doi.org/10.2217/epi-2016-0002.
Kuznetsova, A., Brockhoff, P.B., Christensen, R.H.B., 2017. lmerTest package: tests in linear mixed effects models. J. Stat. Softw. 82 (13). https://doi.org/10.18637/jss.v082.i13.
Lenth, R., 2024. emmeans: Estimated Marginal Means, Aka Least-Squares Means. R package version 1.10.5. https://CRAN.R-project.org/package=emmeans.
Martines, E., Brun, P., Cavazzana, R., Cordaro, L., Zuin, M., Martinello, T., Gomiero, C., Perazzi, A., Melotti, L., Maccatrozzo, L., Patruno, M., Iacopetti, I., 2020. Wound healing improvement in large animals using an indirect helium plasma treatment. Clin. Plasma Med. 17–18. https://doi.org/10.1016/j.cpme.2020.100095.
Morabit, Y., Hasan, MI., Whalley, RD., Robert, E., Modic, M., Walsh, JL. 2021. A review of the gas and liquid phase interactions in low-temperature plasma jets used for biomedical applications. Eur. Phys. J. D 75, 32. doi:https://doi.org/10.1140/epjd/s10053-020-00004-4.
Mosmann, T., 1983. Rapid colorimetric assay for cellular growth and survival: application to proliferation and cytotoxicity assays. J. Immunol. Methods 65 (1-2), 55–63. https://doi.org/10.1016/0022-1759(83)90303-4.
Motain, H., Recek, N., Rogelj, B., 2021. Intracellular responses triggered by cold atmospheric plasma and plasma-activated media in cancer cells. Molecules 26 (5), 1336. https://doi.org/10.3390/molecules26051336.
Narita, M., Nunez, S., Heard, E., Narita, M., Lin, A.W., Hearn, S.A., Spector, D.L., Hannon, G.J., Lowe, S.W., 2003. Rb-mediated heterochromatin formation and silencing of E2F target genes during cellular senescence. Cell 113, 703–716. https://doi.org/10.1016/S0092-8674(03)00401-X.
Nicol, M.J., Brubaker, T.R., Honish 2nd, B.J., Simmons, A.N., Kazemi, A., Geissel, M.A., Whalen, C.T., Siedlecki, C.A., Bilén, S.G., Knecht, S.D., Kirimanjeswara, G.S., 2020. Antibacterial effects of low-temperature plasma generated by atmospheric-pressure plasma jet are mediated by reactive oxygen species. Sci. Rep. 10 (1), 3066. https://doi.org/10.1038/s41598-020-59652-6.
Otero-Sabio, C., Giacomello, M., Centelleghe, C., Caicci, F., Bonato, M., Venerando, A., Graïc, JM., Mazzariol, S., Finos, L., Corain, L., Peruffo, A. 2022. Cell cycle alterations due to perfluoroalkyl substances PFOS, PFOA, PFBS, PFBA and the new PFAS C6O4 on bottlenose dolphin (*Tursiops truncatus*) skin cell. Ecotoxicol. Environ. Saf. 244, 113980. doi:https://doi.org/10.1016/j.ecoenv.2022.113980.
Peruffo, A., Bassan, I., Gonella, A., Maccatrozzo, L., Otero-Sabio, C., Iannuzzi, L., Perucatti, A., Pistucci, R., Giacomello, M., Centelleghe, C., 2025. Establishment and characterization of the Cuvier's beaked whale (*Ziphius cavirostris*) myogenic cell line. Res. Vet. Sci. 182, 105471. https://doi.org/10.1016/j.rvsc.2024.105471.
Poirier, M.C., 2021. DNA damage in cetaceans: a mini review. Mutat. Res. Genet. Toxicol. Environ. Mutagen. 870-871, 503392. https://doi.org/10.1016/j.mrgentox.2021.503392.
R Core Team, 2024. R: A Language and Environment for Statistical Computing. R Foundation for Statistical Computing, Vienna, Austria. https://www.R-project.org/.
Redza-Dutordoir, M., Averill-Bates, D.A., 2016. Activation of apoptosis signaling pathways by reactive oxygen species. Biochim. Biophys. Acta 1863 (12), 2977–2992. https://doi.org/10.1016/j.bbamcr.2016.09.012.
Roukos, V., Pegoraro, G., Voss, T.C., Misteli, T., 2015. Cell cycle staging of individual cells by fluorescence microscopy. Nat. Protoc. 10, 334–348. https://doi.org/10.1038/nprot.2015.016.
Roux, S., Marchès, A., Galiacy, S., Merbahi, N., Simon, M., 2025. Biological solutions activated by cold plasma at atmospheric pressure: a new therapeutic approach for skin wound healing. Biomed. Pharmacother. 186, 118001. https://doi.org/10.1016/j.biopha.2025.118001.
Schorpp, K., Rothenaigner, I., Maier, J., Traenkle, B., Rothbauer, U., Hadian, K., 2016. A multiplexed high-content screening approach using the chromobody technology to identify cell cycle modulators in living cells. J. Biomol. Screen. 21 (9), 965–977.
Segura-Göthlin, S., Fernández, A., Arbelo, M., Andrada Borzollino, M.A., Felipe-Jiménez, I., Colom-Rivero, A., Fiorito, C., Sierra, E., 2023. Viral skin diseases in odontocete cetaceans: gross, histopathological, and molecular characterization of selected pathogens. Front. Vet. Sci. 10, 1188105. https://doi.org/10.3389/fvets.2023.1188105.
Solan, M., Senthilkumar, S., Aquino, G., Bruce, E., Lavado, R., 2022. Comparative cytotoxicity of seven per- and polyfluoroalkyl substances (PFAS) in six human cell lines. Toxicology 477.
Toms, C.N., Stone, T., Och, T., 2021. Skin lesion and mortality rate estimates for common bottlenose dolphin (*Tursiops truncatus*) in the Florida Panhandle following a historic flood. PLoS One 16. https://doi.org/10.1371/journal.pone.0257526.
Tornin, J., Labay, C., Tampieri, F., Ginebra, M.P., Canal, C., 2021. Evaluation of the effects of cold atmospheric plasma and plasma-treated liquids in cancer cell cultures. Nat. Protoc. 16, 2826–2850. https://doi.org/10.1038/s41596-021-00521-5.
Tresp, H., Hammer, M.U., Winter, J., Weltmann, K.-D., Reuter, S., 2013. Quantitative detection of plasma-generated radicals in liquids by electron paramagnetic resonance spectroscopy. J. Phys. D. Appl. Phys. 46, 435401. https://doi.org/10.1088/0022-3727/46/43/435401.
Turrini, E., Laurita, R., Stancampiano, A., Catanzaro, E., Calcabrini, C., Maffei, F., Gherardi, M., Colombo, V., Fimognari, C., 2017. Cold atmospheric plasma induces apoptosis and oxidative stress pathway regulation in t-lymphoblastoid leukemia cells. Oxidative Med. Cell. Longev. https://doi.org/10.1155/2017/4271065.
Uchida, Giichiro, Nakajima, Atsushi, Ito, Taiki, Takenaka, Kosuke, Kawasaki, Toshiyuki, Koga, Kazunori, Shiratani, Masaharu, 2016. Effects of nonthermal plasma jet irradiation on the selective production of H2O2 and NO2− in liquid water. Phys. Plasmas. 23 (12). https://doi.org/10.1063/1.4968568.
Vakifahmetoglu, H., Olsson, M., Zhivotovsky, B., 2008. Death through a tragedy: mitotic catastrophe. Cell Death Differ. 15, 1153–1162. https://doi.org/10.1038/cdd.2008.47.
Van Bressem, M.F., Van Waerebeek, K., Raga, J.A., 1999. A review of virus infections of cataceans and the potential impact of morbilliviruses, poxviruses and papillomaviruses on host population dynamics. Dis. Aquat. Org. 38, 53–65. https://doi.org/10.3354/dao038053.
Van Bressem, M.F., Félix, F., Van Waerebeek, K., 2024. A review of lobomycosis and lobomycosis-like skin disease in cetaceans worldwide, with new data from the Gulf of Guayaquil, Ecuador. Med. Mycol. 62. https://doi.org/10.1093/mmy/myae089.
Virard F, Cousty S, Cambus J.P, Valentin A, Kémoun P, Clément F. 2015. Cold atmospheric plasma induces a predominantly necrotic cell death via the microenvironment. PLoS One 10(8):e0133120. doi:https://doi.org/10.1371/journal.pone.0133120.
Wang, H., Jia, X.Z., Sui, C.J., Zhao, Y.P., Mei, Y.F., Zheng, Y.N., Zhang, Z.Y., 2014. Effects of thapsigargin on the proliferation and survival of human rheumatoid arthritis synovial cells. Sci. World J., 605416 https://doi.org/10.1155/2014/605416.
Wu, Y., Yu, S., Zhang, X., Wang, X., Zhang, J., 2023. The regulatory mechanism of cold plasma in relation to cell activity and its application in biomedical and animal husbandry practices. Int. J. Mol. Sci. 24, 7160. https://doi.org/10.3390/ijms24087160.
Zhai, S.Y., Kong, M.G., Xia, Y.M., 2022. Cold atmospheric plasma ameliorates skin diseases involving reactive oxygen/nitrogen species-mediated functions. Front. Immunol. https://doi.org/10.3389/fimmu.2022.868386.
Zhang, H., Zhang, C., Han, Q., 2023. Mechanisms of bacterial inhibition and tolerance around cold atmospheric plasma. Appl. Microbiol. Biotechnol. 107 (17), 5301–5316. https://doi.org/10.1007/s00253-023-12618-w.